International Journal of Machine Tools & Manufacture 193 (2023) 104088

Contents lists available at ScienceDirect

International Journal of Machine Tools and Manufacture

journal homepage: www.elsevier.com/locate/ijmactool

Research Article

Towards understanding the crack suppression mechanism in brittle materials with high grinding speed at different temperatures

Jianqiu Zhang [a], Xuekun Shang [a], BinBin He [a,**], Bi Zhang [a,*]

[a] Department of Mechanical and Energy Engineering, Southern University of Science and Technology, Shenzhen, 518055, China

ARTICLE INFO

Handling Editor: Prof Dragos Axinte

Keywords:
High-speed grinding
Temperature-assisted grinding
Brittle materials
Crack nucleation
Crack suppression

ABSTRACT

Ductile-regime grinding has been used to eliminate the formation of subsurface cracks by setting an extremely small depth of cut (DOC). The critical DOC is affected by multiple factors, including the grinding speed and material temperature. The underlying mechanism of DOC affected by the grinding speed is still unclear. To reveal the role of grinding speed and material temperature during the formation of cracks, we conducted a series of single-point grinding experiments with the different grinding speeds (26.7–192.3 m/s) and the initial material temperatures (25–200 °C). The experimental results showed that cracks were suppressed with an increase in the grinding speed and initial material temperature even when the DOC was much deeper than the critical DOC determined by the ductile-regime grinding. To understand the mechanisms underlying crack nucleation and suppression, we conducted systematic molecular dynamics simulations. Both simulation and experimental results showed that a crack can be formed by a single slip band. The crack nucleates from a microvoid within the slip band. With the aid of the local tensile stress on one side of the slip band tip, the crack nucleation forms an opening crack. The crack suppression is primarily caused by the high-pressure field during high-speed grinding, where the high-pressure field superposes the local tensile stress to forming a compressive stress state that prevents crack nucleation. In addition, the brittle-ductile transition is induced by the high temperature on the surface during high-speed grinding. This study provides insights into building the DOC criterion for different grinding speeds and temperatures based on a 'bottom-up' approach.

1. Introduction

Grinding is an important technique used to increase the surface integrity of structural and functional components in a wide range of engineering applications such as microchip manufacturing. However, the grinding process can introduce various defects including cracks in the subsurface of the brittle materials. The cracks impair the service behavior of components and require sophisticated mechanical or electrochemical polishing to be removed. Therefore, it is important to suppress the formation of cracks in the subsurface of machined materials by grinding.

To suppress cracks during the grinding of brittle materials, ductile-regime grinding [1], which stems from a mechanical model based on ceramic indentation [2], is frequently employed. The concept of ductile-regime grinding indicates that there is a critical depth of cut (DOC) below which the grinding of brittle materials is similar to that of ductile materials. This treatment can be scientifically explained by the principle that the atoms near a free surface require lower energies to form dislocations compared with the atoms in a bulky material [3], which is attributed to the material near a free surface being more compliant. Nevertheless, the accuracy of the ductile-regime theory still needs to be improved, because it is a 'top-down' model derived from macro-physical variables, including hardness, toughness and elastic modulus, almost irrespective of the interactions between the loading and microstructural evolution. Additionally, the critical DOC is affected by the different grinding conditions [4], including the material temperature, abrasive-particle geometry, grinding speed, crystal orientation [5] and lubrication [6]. However, these conditions are not considered in the ductile-regime theory, and thus there is a need to gain a deep understanding on the mechanism of each grinding condition influencing the critical DOC.

To elevate the critical DOC, the material temperature was increased to suppress cracks during the grinding of brittle materials. The underlying reason is that atoms at higher temperatures are thermally activated

* Corresponding author.
** Corresponding author.
E-mail addresses: hebb@sustech.edu.cn (B. He), zhangb@sustech.edu.cn (B. Zhang).

https://doi.org/10.1016/j.ijmachtools.2023.104088
Received 30 April 2023; Received in revised form 24 October 2023; Accepted 27 October 2023
Available online 9 November 2023

with higher kinetic energy to overcome energy barrier, and thus tend to form dislocations instead of cracks [3]. The temperature of materials during grinding can be increased using several approaches, including lasers and heaters. A surface finish of optical quality was obtained on surface (111) of a monocrystalline silicon (MS) workpiece using fiber laser with a power of 20 W coupled with single point diamond turning with a DOC of 2 μm [7]. In addition, a laser-coupled single-point scratch was used to study the critical DOC of MS at different temperatures. The enhancement of the critical DOC of MS under laser irradiation was confirmed by Chen et al. [8], and a similar approach was employed to specifically study the relationship between the laser power and critical DOC [9]. They found that the critical DOC increased from 84 nm to 221 nm when the laser power was increased from 0 W to 40 W. However, the pressure caused by the laser [10] on the surface was not mentioned in these studies, which probably influenced the DOC. In contrast, a heater coupled with a single-point scratch was used to investigate the critical DOC of soft-brittle materials, such as in the work of Liu et al. [11], who investigated the critical DOC of KH_2PO_4. They found that the critical DOC of KH_2PO_4 scratched at 170 $^{\circ}C$ reached to 3.6 μm, which was 8.6 times the critical DOC at room temperature. Nevertheless, the temperature elevated by a heater is relatively low that limits the applications of this heating approach because many brittle materials are not sensitive to a temperature range of 25–200 $^{\circ}C$. In addition, the crack formation process is not discussed in detail in the aforementioned studies.

Abrasive particle geometry also influences the formation of cracks during grinding of brittle materials. Axinte et al. [12] employed abrasive particles with three shapes to grind sapphire, suggesting that abrasive particles with a circular base frustum performed better in suppressing cracks than triangular and square base frustums. The rake angle of abrasive particles is another factor that affects crack formation during the grinding of brittle materials. Yan et al. [13] employed abrasive particles with distinct rake angles in single-point scratch of MS workpieces, and the results showed that the optimum rake angle was -45° and yielded the deepest critical DOC. This finding was supported by Mohammadi et al. [7], although the optimum rake angle in their study was -25°. An excessively large negative rake angle may cause rubbing of the ground surface, which may impair surface integrity. Zhang et al. [14] studied the crack suppression mechanism with a negative rake angle by carrying out smoothed particle hydrodynamics (SPH) simulations. They found that the pressure under the abrasive particles played an important role in crack suppression. Nevertheless, the SPH method cannot determine the complex microstructural evolution of the subsurface during the grinding process. Therefore, the precise role of pressure in controlling the microstructural evolution, and thus the suppression of cracks in the subsurface of brittle materials caused by pressure during grinding, remains unclear.

In the past decades, high-speed grinding has been carried out to suppress the formation of cracks during the grinding of brittle materials. Zhang et al. [15] conducted experiments of single-point scratches on alumina with a speed of 26.7 m/s and investigated the surface integrity of ground sample. The results showed that cracks remained beneath the surface, although the surface after grinding was quite smooth. Thus, a smooth surface cannot be regarded as a criterion for determining whether ductile grinding is achieved. In other words, cracks in the subsurface are vital and must be carefully examined. Schinker [16] observed severe plastic deformation instead of cracks on the ground surface of glass when the grinding speed reached 100 m/s. Severe plastic deformation was observed by Huang et al. [17] when the grinding speed was increased to 160 m/s during the grinding of silicon nitride. Unfortunately, the microstructural evolution in the subsurface was not examined by Schinker [16] and Huang et al. [17], and the underlying mechanism of crack suppression influenced by the grinding speed is still not completely understood.

Many microstructures related to crack formation in the subsurface of brittle materials were observed in the ground samples. The cracks nucleate at locations under the amorphous layer where massive dislocations are concentrated during the grinding of MS [18]. Li et al. [19] found that the intersection of the slip bands served as the origin of crack nucleation. These facts imply that the crack nucleation is triggered by plastic deformation. Furthermore, Li et al. [19] found that the stacking faults and dislocations reside in the slip bands, while Liu et al. [11] found that microvoids were aligned within the slip bands. During plastic deformation, these atomic defects are potential triggers of crack nucleation. It is worth noticing that the classical crack formation theory of ductile materials states that the growth and coalescence of microvoids trigger crack nucleation [20,21]. Furthermore, Rice et al. [22] and Huang [23] reported that negative pressure (positive hydrostatic stress) drives the growth of the microvoids. However, to the best of our knowledge, the relationships between these defects are still not completely understood, and no studies have presented a complete picture of the crack formation process. Therefore, in situ experiments and simulations are required to improve the understanding of the microstructural evolution process.

To understand crack formation and suppression in brittle materials during grinding at various speeds, in this study, we conducted a series of experiments along with large-scale molecular dynamic (MD) simulations using MS as the model material. The grinding speeds and initial material temperatures (IMTs) of MS in the experiments were within a range of 26.3–192.3 m/s and 25–200 $^{\circ}C$, respectively. The experiments showed that cracks can be generated from a single slip band, which was verified by the MD simulations. In addition, negative pressure plays a vital role in microvoid formation and growth, which cause crack nucleation, and the high-pressure field during high-speed grinding results in crack suppression. This study provides the fundamentals at the microscopic level to build an analytical model based on 'bottom-up' approach to determine the critical conditions for crack suppression during grinding of brittle materials.

2. Experimental methodology

To investigate the role of grinding speed on the formation of crack in the subsurface, an in-house grinding machine was developed, as Fig. 1 (a). The MS workpiece, heater, and flat K-type thermocouple were sequentially stacked and clamped to the end surface of the cooling platform. The cooling platform was hollow with a cooling hole (Fig. 1 (b)). Two orifices were drilled at the two opposite walls of the cooling hole and used for the inflow and outflow of the cooling air. Cooling air was supplied to the cooling hole at a constant flow rate to prevent platform heating, which could cause thermal expansion. The circuit diagram of the temperature control system is shown in Fig. 1(c). A proportional-integral-derivative (PID) controller was used to receive the temperature signal transmitted by the K-type thermocouple. An electric relay was used to control the power-on time of the heater so that the heating temperature can be stabilized at the target. Because a slight difference existed between the temperature measured by the flat K-type thermocouple and the IMT measured by another K-type thermocouple mounted on a handheld device, the target temperature set on the temperature control system was offset by the temperature difference between the measured IMT and the temperature measured by the flat K-type thermocouple. This operation was repeated several times before the experiments until IMT stabilized at the target. A tool-presetting operation was performed to examine the shift in the MS surface position induced by thermal fluctuations, which was repeated several times to confirm that the position of the MS surface shift was less than 1 μm within 10 min. This shift satisfied our requirements because each grinding experiment required only a few seconds to complete.

On the spindle side, a cone-shaped diamond abrasive particle with a nose radius of 19 μm was welded onto a rod inserted into a carbon fiber wheel (Fig. 1(a)). The carbon fiber wheel was mounted on a spindle, which was capable of rotating at a revolution speed of 60,000 rpm with an axial error motion of less than 0.1 μm. The abrasive particle rotated around the rotation axis of the spindle, and the rotation radius of the

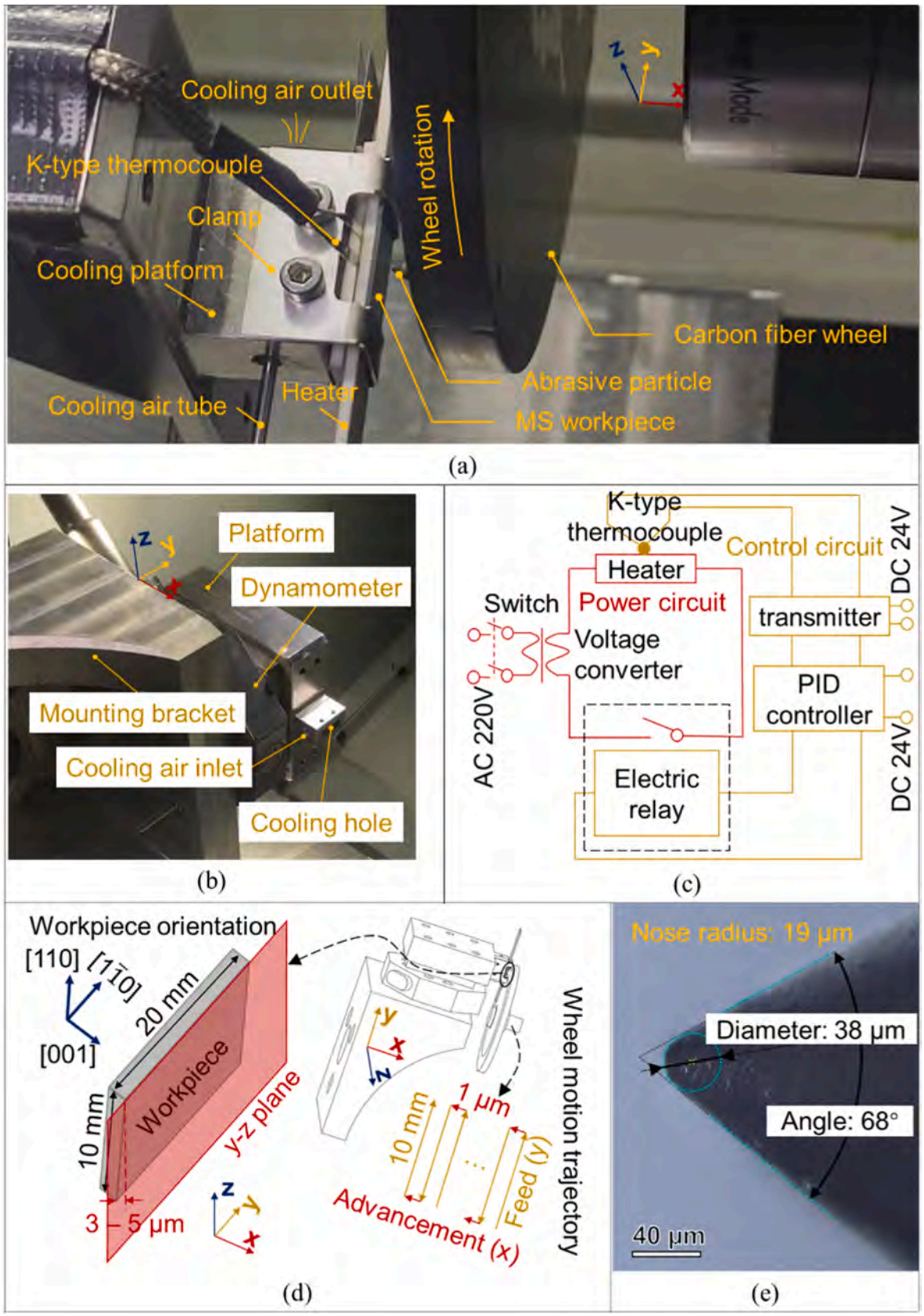

Fig. 1. Setup of the single-point grinding experiments. (a) Assembly of the experimental apparatus. (b) Close-up view of the platform. Note that the cooling hole is crucial to prevent thermal expansion of the platform during the heating process. (c) Circuit diagram of the temperature control system. (d) Schematic of the grinding strategy. The DOC was determined by the advancement motion. Note that the inclination angle was ~0.017°–0.028°, which was very small, and the inclination angle did not affect grinding on (001) surface. (e) Nose radius of abrasive particle.

abrasive particle was 52 mm. Before the experiment, the dynamic balance of the carbon fiber wheel was conducted at the rotational speeds used in the experiment, and the translation trajectory of the wheel spindle is shown in Fig. 1(d). The translation can be divided into two successive motions: (1) an advancement motion of 1 μm along the x-axis, and (2) a feed motion along the y-axis. The feed distance was set to 10 mm.

Taper grinding was used to alleviate shocks during grinding. The MS workpieces with dimensions of 10 mm × 20 mm × 0.5 mm were fixed at a small inclination angle (0.017°–0.028°) with respect to the x-y plane (Fig. 1(d)). In the experimental setup, the angle was realized by adjusting the difference between the upper edge and the lower edge to be 3–5 μm, as Fig. 1(d). Considering the negligible inclination angle, the small advancement motion (~1 μm), and the fine nose radius (19 μm) (Fig. 1(e)), the incline in the present experimental setup could not affect the grinding status on face (001). The crystalline orientation of the workpiece is illustrated in Fig. 1(d). The grinding direction was along the crystal orientation [110]. Because the trajectory of the abrasive particle is a curve, a deviated angle exists between the grinding direction and the crystal orientation [110]. Based on the geometric relationship, the maximum deviated angle was estimated to be 5.5°. Although MS is anisotropic, the difference of the critical DOC of the grinding along the crystal orientation [110] and the grinding along the maximum deviated direction is 5 % [5]. Therefore, the influence of deviation in the grinding direction was neglected from the analysis.

Ten experiments were conducted, and the details of the experimental grinding parameters are presented in Table 1. Five experiments were conducted at room temperature with a grinding speed ranging from 26.7 m/s to 192.3 m/s classified as the room-temperature group (RTG). The other five experiments were conducted at 200 $^{\circ}C$ with the same grinding speed range and classified as the high-temperature group (HTG). To ensure that the grinding path gap was the same for both groups, the feed rate of each experiment was set such that the ratio of the grinding speed to the feed rate was equal in all experiments [24].

The microstructures beneath the ground surface were characterized by FEI Talos F200X G2 transmission electron microscopy (TEM) at 200 kV using the scanning transmission electron microscopy (STEM) mode. The TEM samples were fabricated by FEI Helios 600i focused ion beam (FIB) equipment using a typical "lift-out" method [25].

3. Results

3.1. Topographies of the ground surfaces

The topographies of the ground surfaces of the RTG and HTG are presented in two columns of Fig. 2 in ascending order of the grinding speed. It can be seen that the chipping degree caused by cracking was suppressed with an increase in the grinding speed except for Case 5. Therefore, the experiment for Case 5 was repeated three times. Unfortunately, the abrasive particle fractured in all of the three experiments. By comparing the cases in the RTG and HTG with identical grinding speeds, the chipping degree decreased with an increase in the IMT. Based on the ranges of the IMT and grinding speed, it can be deduced that the grinding speed plays a dominant role in suppressing cracks. In addition, some of the cracks ceased to propagate within the subsurface, as substantiated by the STEM observations described in Section 3.2.

STEM was employed to further examine the subsurface cracks. The STEM samples were fabricated using the FIB equipment. Samples with a width of 6 μm and depth of 6 μm were extracted from Cases 1 and 10 followed by a thinning process using Ga + ion beam. In the final milling step, a beam current of 24 pA operated at 30 kV was used. The orientations of the two samples are marked in Fig. 2(a) and (j). The sample surface was perpendicular to the grinding direction.

The surface roughness (Sa) was measured for each case as Fig. 3. For the RTG and HTG cases, the overall trend of the surface roughness decreased with an increase in the grinding speed, except for Case 5, where the abrasive particle fractured. There were no significant differences in the surface roughness observed between the RTG and HTG.

3.2. Characterization of subsurface damage

The overall landscape of the subsurface damage for Case 1 is shown in Fig. 4(a). It can be seen that cracks initiate from the slip bands and propagate to the lateral side. The region of interest is enlarged in Fig. 4 (b) that shows slip bands propagated from the surface to the subsurface, forming an angle of 54.7° with respect to the horizontal direction. The angle between the crack and slip bands was 70.5° and a crack closure occurred at the crack tip. A number of dislocations with a bow shape glided downward; the amorphous materials piled up at the surface adjacent to the grinding groove. It is worth noting that the cracks were formed from single slip bands. Fig. 4(c) shows the microstructure adjacent to the grinding groove, and a bright band can be observed, as enlarged in Fig. 4(d). Fast Fourier transformation (FFT) was applied to the selected region in Fig. 4(d). FFT #1 indicates that the metallurgical structure within the band is amorphous, while FFT #2 shows the material adjacent to the band has a cubic diamond structure. In addition, in Fig. 4(b), the nucleation location of the longest crack implies that crack nucleation is relative to slip bands. This finding differs from those of previous studies, which showed that cracks were initiated where massive dislocations were concentrated [26] or where slip bands intersected [19].

The subsurface damage for Case 10 is shown in Fig. 5. Fig. 5(a) shows the landscape of the subsurface damage, and it can be seen that the number of cracks in the subsurface for Case 10 is significantly less than that in the subsurface for Case 1. In addition, the crack length for Case 10 appeared to be shorter than that in the subsurface for Case 1. Thus, the cracks in the subsurface for Case 10 were suppressed. The region of interest in Fig. 5(a) is enlarged as shown in Fig. 5(b). In Fig. 5(b), the amorphous layer is on the top and extremely fine grains (EFG) were wrapped by the amorphous layer. These EFGs likely come from the chips, the outer layer of which is amorphous causing the chips to flow on the surface during grinding. In addition, the flowability of amorphous materials may cause chip spheroidization. The EFG was enlarged in Fig. 5(c). Nanotwinning was observed within the EFGs (Fig. 5(c)), which was confirmed by the diffraction pattern FFT#1 (Fig. 5(e)). The amorphous structure surrounding the EFG can be confirmed by FFT#2 (Fig. 5 (d)). It shall be highlighted that massive dislocations forming dislocation walls were distributed in deeper locations, as shown in Fig. 5(b). The short slip bands and crack were initiated within the region of massive dislocations, implying that the crack was formed by dislocation interactions. Furthermore, the crack formed at angle of 54.7° with respect to the horizontal direction.

The number of cracks in the subsurface for Case 10 was fewer than that for Case 1. To confirm this trend, we fabricated another FIB sample from the workpiece of Case 10. The landscape is shown in Fig. 6(a), which is similar to that shown in Fig. 5(a). No crack was found in the landscape, which further confirmed that cracks suppressed with an

Table 1
Parameters of single-point grinding experiments.

Case number	Grinding speed (m/s)	Feed rate (mm/min)	DOC (μm)	Temperature ($^{\circ}C$)
1	26.7	26.7	1	25
2	53.4	53.4	1	25
3	106.8	106.8	1	25
4	160.2	160.2	1	25
5	192.3	192.3	1	25
6	26.7	26.7	1	200
7	53.4	53.4	1	200
8	106.8	106.8	1	200
9	160.3	160.2	1	200
10	192.3	192.3	1	200

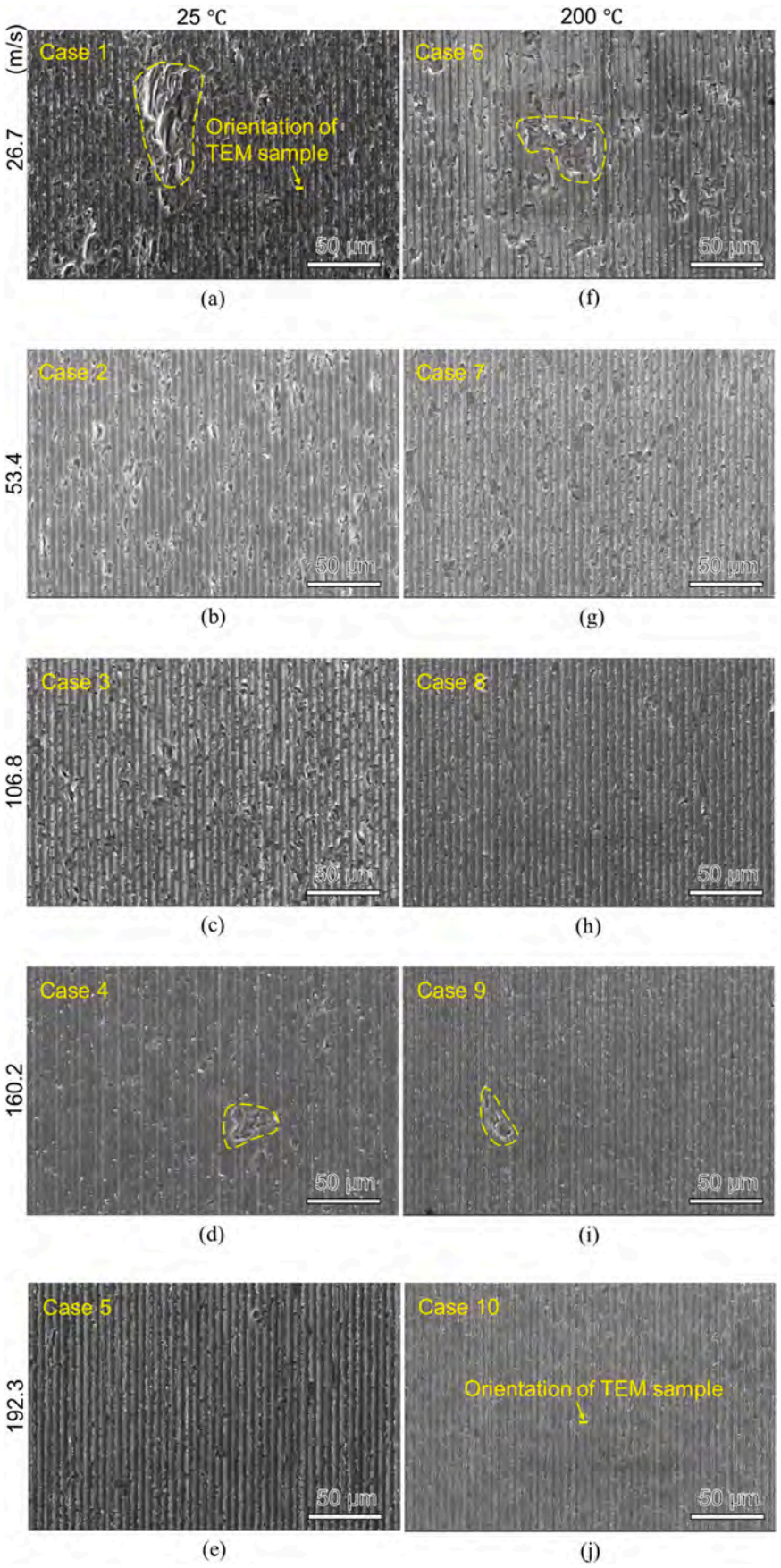

(caption on next page)

Fig. 2. Ground surface topographies of ten cases characterized by scanning electron microscopy. Two columns ((a)–(e) and (f)–(j)) represent RTG (25 °C) and HTG (200 °C), respectively, listed in ascending order of the grinding speed. The yellow dashed lines indicate large chippings. Note that the chipping area decreases with an increase in the grinding speed. The ground surface of Case 5 was rough due to fracture of the abrasive particle. (For interpretation of the references to colour in this figure legend, the reader is referred to the Web version of this article.)

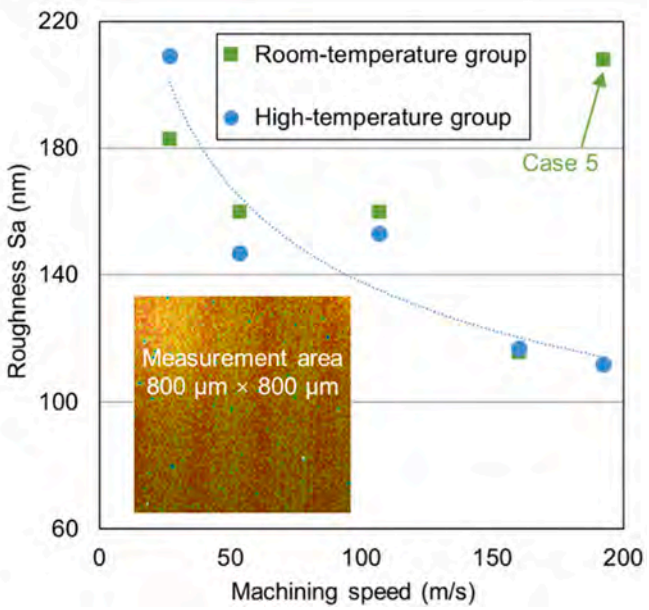

Fig. 3. Variations in surface roughness (Sa) in RTG and HTG measured using a white light interferometer. The surface roughness was sampled within a measurement area of 800 μm × 800 μm. The surface roughness of the HTG showed a decreasing trend with an increase in the grinding speed. Note that the surface roughness for Case 5 was high due to fracture of the abrasive particle.

increase in grinding speed. Fig. 6(b) is the energy-dispersive spectroscopy of the local region in Fig. 6(a), which clearly illustrates that amorphous silicon covered the EFGs. Because the Moire pattern disturbs the identification of the detailed microstructural evolution in Fig. 6(a), the microstructural evolution based on Fig. 6 is not discussed further in this article.

The orientations of the cracks and slip bands in Figs. 4 and 5 were related to the crystalline orientation of the MS. The slip bands and crack in Fig. 4(b) and the crack in Fig. 5(b) formed at an angle of 54.7° with respect to the horizontal direction. These angles were consistent with the angle marked in the unit cell of the MS in Fig. 7(b). The angle in Fig. 7(b) was formed by the (111) and (001) planes, as in Fig. 7(a). Therefore, the angles measured in the subsurface may imply that the slip bands and cracks in the subsurface are prone to occur on {111} planes, on which slipping and cleavage are easily initiated [27].

3.3. Results of MD simulations

To investigate the mechanism underlying the crack suppression, large-scale MD simulations were performed using a large-scale atomic/molecular massive parallel simulator (LAMMPS). The number of atoms employed in the simulation was more than 8 million, and the simulations were conducted using high-performance computers with 520 central processing units in parallel. The model and essential geometric parameters are shown in Fig. 8. The grinding was arranged orthogonally. The model had a large size in the x-y plane that reached the scale of 10^3 Å, but the length along the z-axis was only 15 Å. Such an arrangement can increase the scale of the model with limited atoms, which can result in complex atom evolutions. Owing to the small number of atoms arranged along the z-axis, periodic boundary conditions were imposed on the atoms on the two side planes perpendicular to the z-axis. To capture cracks, the DOC was set to 775 Å, which was larger than the critical DOC for ductile-regime grinding [28]. The contact surface of the abrasive particle was assumed to be a rigid body. The grinding direction was along the x-axis, corresponding to the crystalline orientation index of [110] (Fig. 8). Newtonian atoms were established to mimic the silicon atom evolution during grinding, thermal reservoir atoms were used to provide heat to stabilize the whole model at the specified temperature, and fixed atoms were used to provide the fixed boundary conditions. The rake and clearance angles were set to −30° and 5.5°, respectively (Fig. 8). The negative rake angle was chosen to mimic the grinding process since a large rake angle (≥40°) would cause a large deformation region, which would require a large model. Therefore, to balance the model size and ensure similarity to the abrasive particle, the rake angle was set to −30°. To save computing resources, the fixed atoms were not exported in the simulation results in this study.

The Stillinger–Weber (S–W) model was employed to mimic the interactions between the silicon atoms of the workpiece (Si–Si) [29]. The S–W model is a three-body potential function concerning the influence of the bond angle and material anisotropy, and thus it is appropriate to be applied in MS and materials with a cubic diamond structure. The mechanical properties predicted by the S–W model are in good agreement with those of the *ab initio* approach [30]. Furthermore, the performance of dynamically capturing cracks of the S–W model was improved by doubling the coefficient λ, which was validated by experiments [31]. We also attempted other three-body potential functions, including original Tersoff [32] and modified Tersoff [33]. Due to their poor performance of capturing cracks, the Tersoff family was abandoned. The interaction between the Si–C (workpiece and diamond abrasive particle) was described using the Tersoff potential [32].

The physical quantities of each atom were calculated using LAMMPS and averaged to obtain a smooth quantity field. These quantities included the strain and stress. The sample of atoms for averaging was obtained from the atoms within a virtual spherical volume [34]. In this study, the radius of the virtual sphere (cutoff radius) was 4 Å. The virial stresses were recalculated by considering the atomic volume change because LAMMPS did not consider the volume change in the virial stress calculation. The atomic volume was evaluated using the Voronoi tessellation method provided by the Voro++ software package (version 0.4.6). For simplicity, the pressure was used to express the hydrostatic stress, which is defined as:

$$p = -\frac{\sigma_{11} + \sigma_{22} + \sigma_{33}}{3} \quad (1)$$

where p is pressure, and σ_{11}, σ_{22}, and σ_{33} are the normal stresses along the x-, y-, and z-axis, respectively. Pressure p was employed as an indirect indicator of the normal stresses that caused crack formation. Any stress concentration induced by high normal stress can be reflected by the pressure p. Using pressure p is convenient because the normal stresses with various directions surrounding the tips of the cracks can be evaluated in global coordinates rather than building local coordinates for observing each normal stress. Before grinding, Berendsen's relaxation method [35] was used to stabilize the temperature of the entire model at the specified temperature. Moreover, the identification of the amorphous structures in the MD simulation results was based on the radial distribution function [36].

The differences between MD simulations and experiments can be summarized in terms of the mechanics and materials science. First, the configuration of the periodic boundary condition along the z-axis is similar to the plane-strain assumption for orthogonal grinding, which

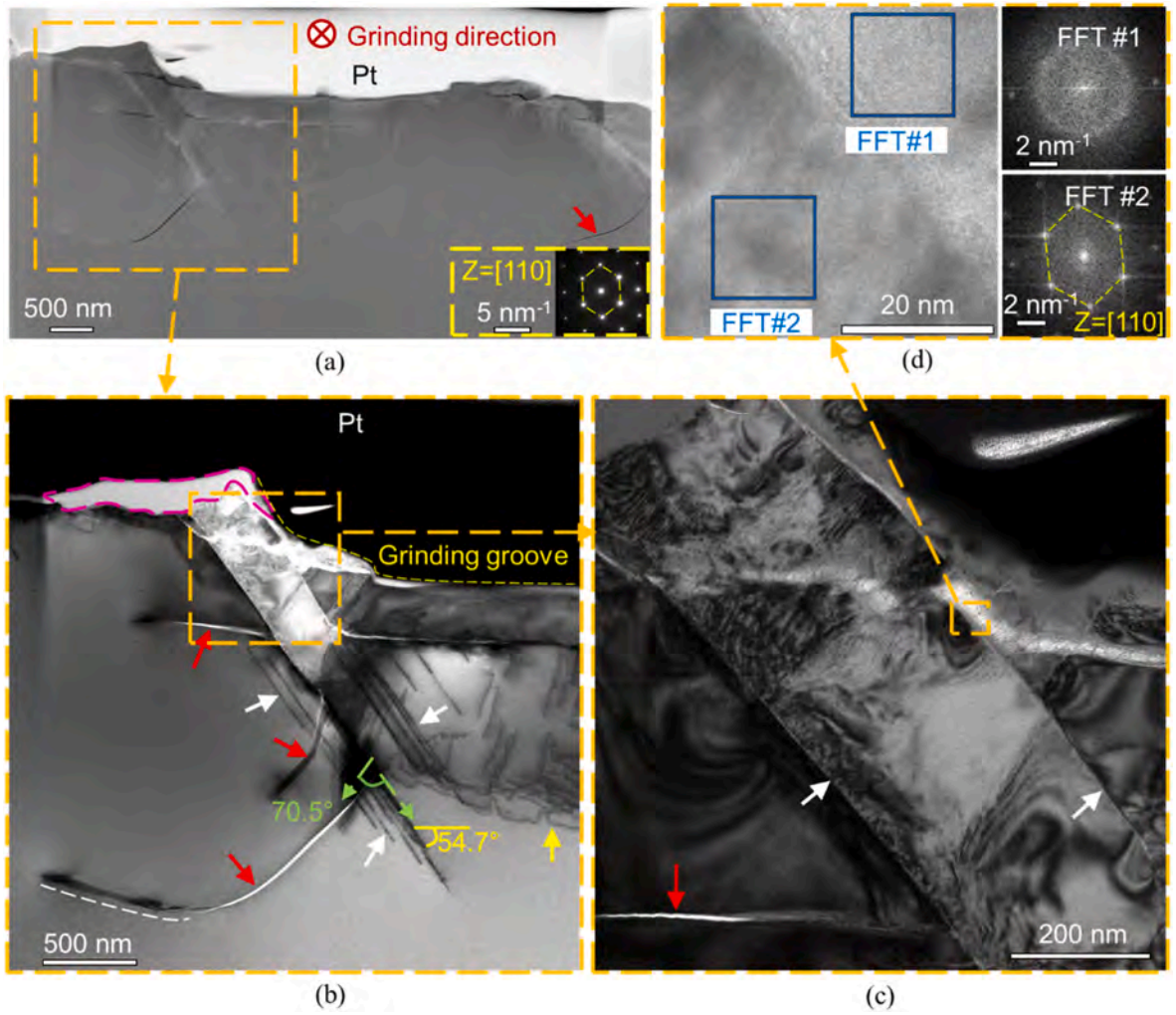

Fig. 4. Subsurface damage for Case 1 characterized by STEM. (a) Overall landscape of the subsurface using a high-angle annular dark-field mode. (b) Enlarged region in (a) captured in dark-field mode. (c) Enlarged region in (b). (d) Amorphous band captured by high-resolution TEM. The magenta dashed circle in (b) represents the amorphous region; the red arrows in (a), (b), and (c) indicate cracks; the white arrows in (b) and (c) denote the slip bands; the yellow arrow in (b) indicates dislocations; the white dashed line in (b) marks crack closure and the angle in (b) between the slip bands and the crack are marked by green dashed arrows. Note that cracks formed from single slip bands, and the angle of 70.5° indicates that both the crack and slip bands lie on the {111} family plane. (For interpretation of the references to colour in this figure legend, the reader is referred to the Web version of this article.)

ignores the shear stresses along the z-axis. Nevertheless, in the experiments, the material in front of the abrasive particle can be pushed to the two sides due to the plowing effect. In addition, the shear stresses along the z-axis influence the subsurface damage, such as the slip bands cause cracks as Fig. 4(b). Second, dislocations cannot completely evolve in a 2.5D model because the model is thin along z direction resulting in a narrow slip plane (i.e., the (111) plane) that cannot fully accommodate dislocation activities, such as dislocations evolving from the Frank-Read source. However, the overall results can reasonably reflect the stress and strain fields, and thus the MD simulations are valid for qualitatively predicting crack nucleation and suppression.

The MD simulation results are presented in Fig. 9. For comparison, all the cases are shown under the condition where the abrasive particle slides by 68 Å. As shown in Fig. 9(a) and (e), long cracks occurred, causing large chipping, which was consistent with the corresponding experimental results (Fig. 2(a) and (f)). In Fig. 9, the crack-suppression trend with increasing grinding speed was consistent with that in the experiments (Fig. 2). In the experiments, the crack suppression for Case 10 was more evident than that for Case 8 (Fig. 2(h) and (j)). However, there were no significant differences in the crack suppression observed between the corresponding simulation cases (Fig. 9(g) and (f)). To further investigate the effect of grinding speed in the simulations, the grinding speed was increased to 534 m/s. In cases with a grinding speed of 534 m/s (Fig. 9(d) and (h)), crack suppression was evident compared with the other simulation cases.

The influence of temperature on the crack formation was not obvious in the simulations, which may be attributed to the fact that the crack formation in the two experimental groups (RTG and HTG) is not significantly different, and such differences are not sufficiently reflected in the MD simulations. In the experiments, crack suppression did not change significantly in the temperature range (25–200 °*C*) compared with the grinding-speed range (26.7–192.3 m/s). The IMT (200 °*C*) of HTG is only 14 % of the melting point of MS, and it does not have significant contribution to crack suppression. Therefore, MD simulations are only used to discuss the influences of stress on crack suppression, and the temperature effect was neglected when discussing the simulation results.

Fig. 10 shows the equivalent shear strain fields and pressure fields arranged in chronological order during grinding for Case 1. An observation window was set in front of the abrasive particle at 88 ps (Fig. 10 (a) and (b)). A slip band propagated from the interface between the abrasive particle and workpiece. A relative slipping motion occurred between the two sides of the slip band. The slipping motion caused compression of the material on the left side of the slip band tip and

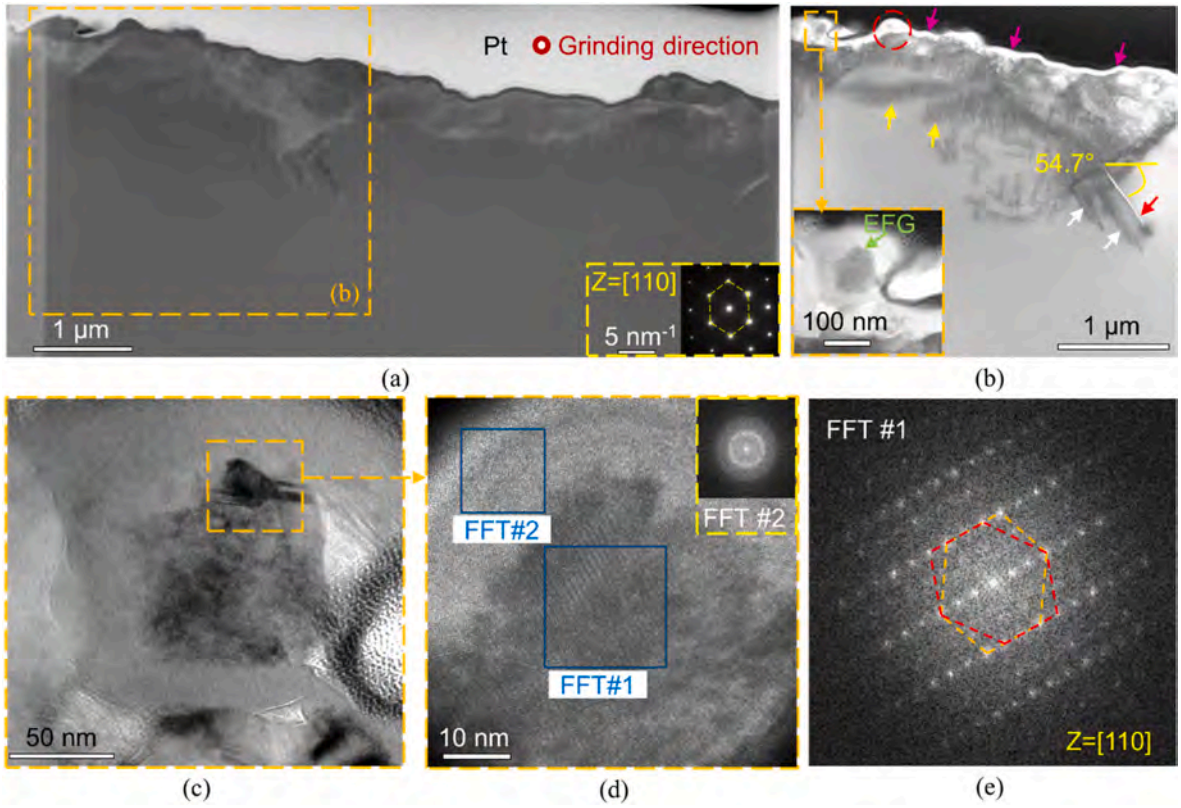

Fig. 5. Subsurface damage for Case 10 characterized by STEM. (a) Overall landscape of the subsurface using a high-angle annular dark-field mode. (b) Enlarged region in (a) captured in dark-field mode. (c) EFG marked in (b). (d) Nanotwinning enlarged from (c). (e) Diffraction pattern of the selected region in (d) obtained from FFT. The magenta arrows in (b) mark amorphous layer; the yellow arrows in (b) indicate the dislocations; the red dashed circle in (b) marks the spheroidized chip; the red arrow in (b) indicates the crack; white arrows in (b) indicate the slip bands. (For interpretation of the references to colour in this figure legend, the reader is referred to the Web version of this article.)

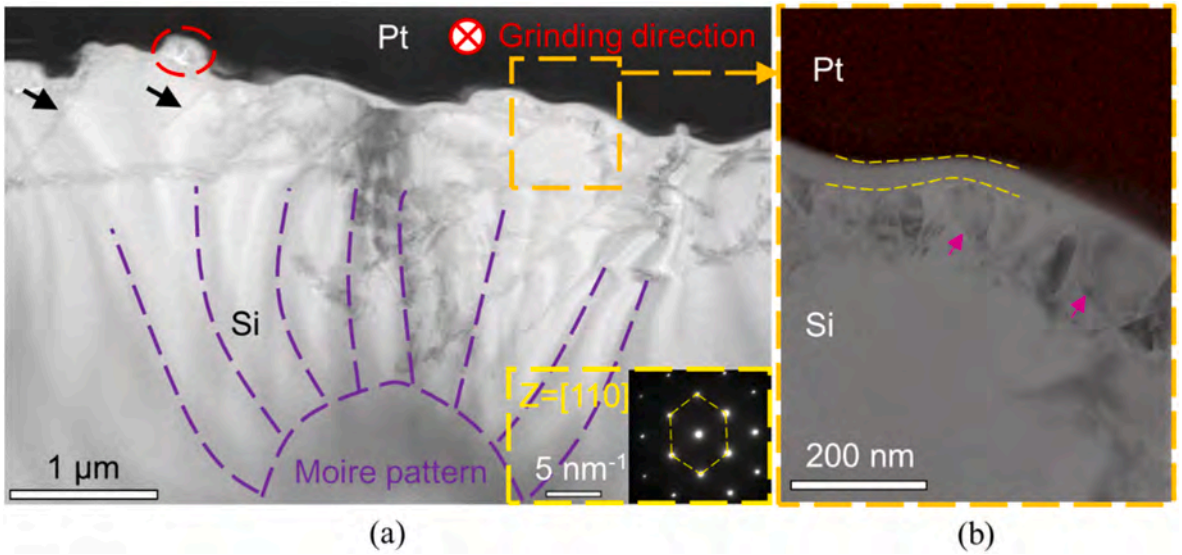

Fig. 6. Crack-free subsurface for Case 10 using STEM in bright-field mode. (a) Landscape of the subsurface. (b) Energy-dispersive spectroscopy of the local region. The red circle in (a) marks spheroidized chip. The black arrows in (a) indicate the slip bands; the yellow dashed lines in (b) illustrate amorphous; the magenta arrows in (b) indicate the EFGs; It shall be highlighted that no cracks were found in this sample. The Moire pattern was observed in the subsurface due to the skewness of the FIB sample. (For interpretation of the references to colour in this figure legend, the reader is referred to the Web version of this article.)

tension on the right side of the slip band tip. The locally concentrated tension results in a microvoid within the slip band, which formed, grew, and further initialized the crack opening (Fig. 10 (c) and (d)). In addition, a pressure concentration of −7 GPa stretched the local material, further forming a lower crack at 160 ps. At 160 ps, the crack was closed, and high pressure occurred, which was enlarged to form a high-pressure field at 208 ps, as shown in Fig. 10(f). The high-pressure field transformed the cubic silicon to the amorphous phase at 264 ps (Fig. 10(i)).

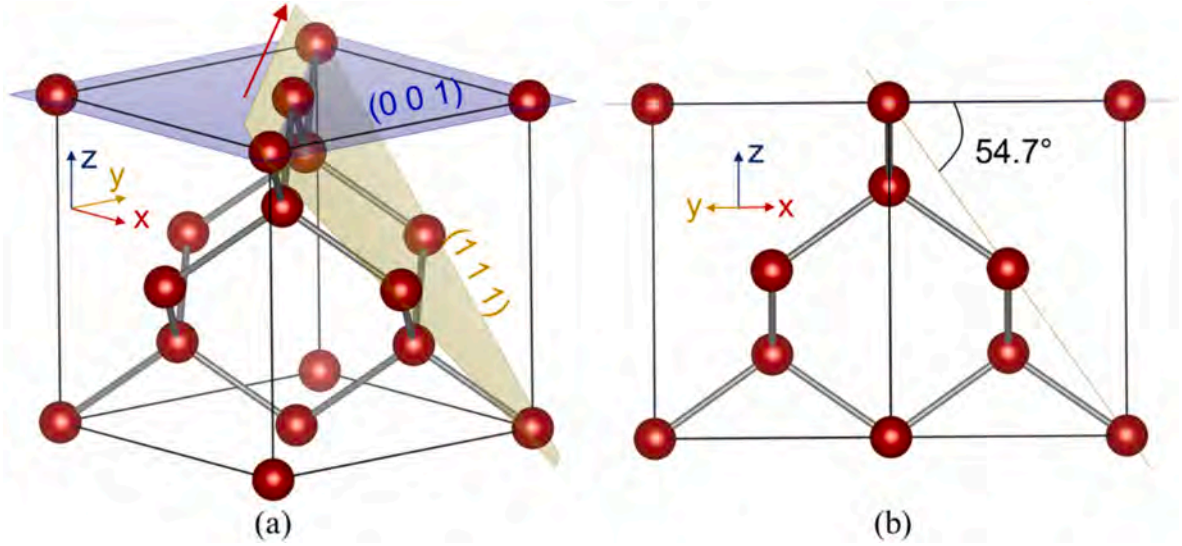

Fig. 7. Structure of the unit cell of monocrystalline silicon. (a) Isometric view of the structure. (b) View along [1 1 0] direction. The red arrow in (a) indicates the grinding direction. (For interpretation of the references to colour in this figure legend, the reader is referred to the Web version of this article.)

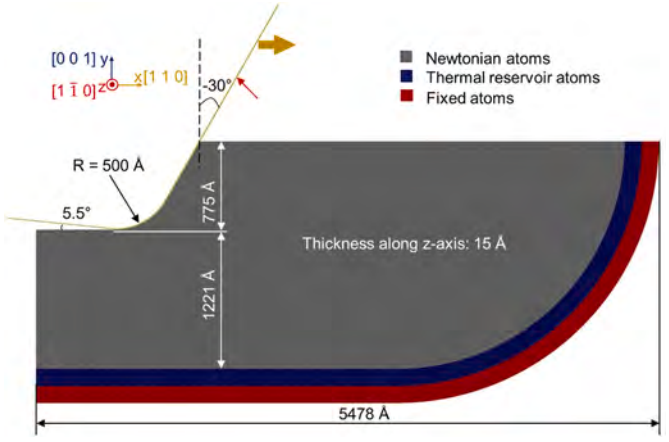

Fig. 8. Major configurations for the large-scale MD simulations. The red arrow indicates the contact surface of the abrasive particle that was assumed to be a rigid body in the simulations while the golden arrow indicates the grinding direction. (For interpretation of the references to colour in this figure legend, the reader is referred to the Web version of this article.)

The crack reopened at 208 ps (Fig. 10(g) and (h)), and it propagated forward at a speed of 1515 m/s (Fig. 10(j)), which was close to the crack propagation speed in glass-like solids [37]. At 336 ps (Fig. 10(k) and (l)), the amorphous layer continued flowing forward; the lower crack tip closed, and the chip spalled from the MS, similar to bending of a cantilever beam. The upper part was under compression whereas the lower part was under tension. The crack was formed by the intersection of two slip bands observed the shear strain field (Fig. 10(e)), which will be explained in Section 4.3.

To complement the experimental subsurface investigation for Case 10 (192 m/s, 200 °*C*), the equivalent strain fields and pressure fields corresponding to Case 10 are chronologically illustrated in Fig. 11. Slip bands and high pressure occurred in the fields (Fig. 11(a) and (b)), and compressive and tensile stress states occurred at the two sides of the slip band tip (Fig. (b)), which was similar to the phenomenon in the initial stage for Case 1. A pressure wave-front occurred in the pressure field, which propagated and caused elastic deformation over a large area. In addition, a surface crack occurred under the flank surface due to stretching of the abrasive particle (Fig. 11(a)). The surface crack closed at 34 ps (Fig. 11(c)). With the propagation of the abrasive particle, the high pressure in front of the abrasive particle formed a larger high-pressure field, and the slip band propagated to deeper locations, forming a tensile field at 34 ps (Fig. 11(d)). The high-pressure and tensile fields respectively covered a part of the slip bands (Fig. 11(d)). Negative pressure in the tensile field resulted in crack nucleation in the form of microvoids (Fig. 11(d)). Crack nucleation further formed a crack at 40 ps (Fig. 11(e) and (f)). No cracks were observed in the high-pressure field. No cracks occurred in front of the abrasive particle at 46 ps (Fig. 11(g) and (h)). The highest pressure in front of the abrasive particle was 0.14 GPa, implying that the materials in front of the abrasive particle were under compression. It shall be noted that the compressive stress state cannot cause cracks in brittle materials.

In both simulations for Case 1 and 10, crack nucleation (Figs. 10(d) and 11(d)) originates from the microvoids residing within the slip bands, which is consistent with the observations of Liu et al. [11]. Furthermore, negative pressure covering the crack nucleation was observed (Fig. 11 (d)), which triggered the material adjacent to the crack nucleation to become tensile. Once the stress exceeds the critical stress for crack formation, a crack is formed.

The equivalent strain fields and pressure fields for Case 12 are shown chronologically in Fig. 12. Numerous slip bands occurred simultaneously at early stages (Fig. 12(a)). A high-pressure field covered the most of the slip bands. With the propagation of the abrasive particle, the slip bands propagated (Fig. 12 (c)), and an elastic pressure wave propagated ahead of high-pressure field (Fig. 12(d)). The pressure wave reached the bottom boundary at 12.4 ps (Fig. 12(f)), and the slip bands did not propagate further toward the outer area of the high-pressure field. At 16.4 ps, the slip bands were still covered by the high-pressure field (Fig. 12(g)). The lowest pressure at that moment was −4 GPa, implying that there was stretching at the lowest pressure region. It is worth noting that the stretching did not cause a crack nucleation. The reason is probably that −4 GPa did not reach the critical fracture stress.

4. Discussion

4.1. Crack nucleation suppressed by the high-pressure field

The pressure in front of the abrasive particle for case 1 was not sufficiently high, and the high-pressure field is not sufficiently large to cover most of the slip bands. Therefore, the negative pressure induced by stretching at one side of the slip band tip caused crack formation in Case

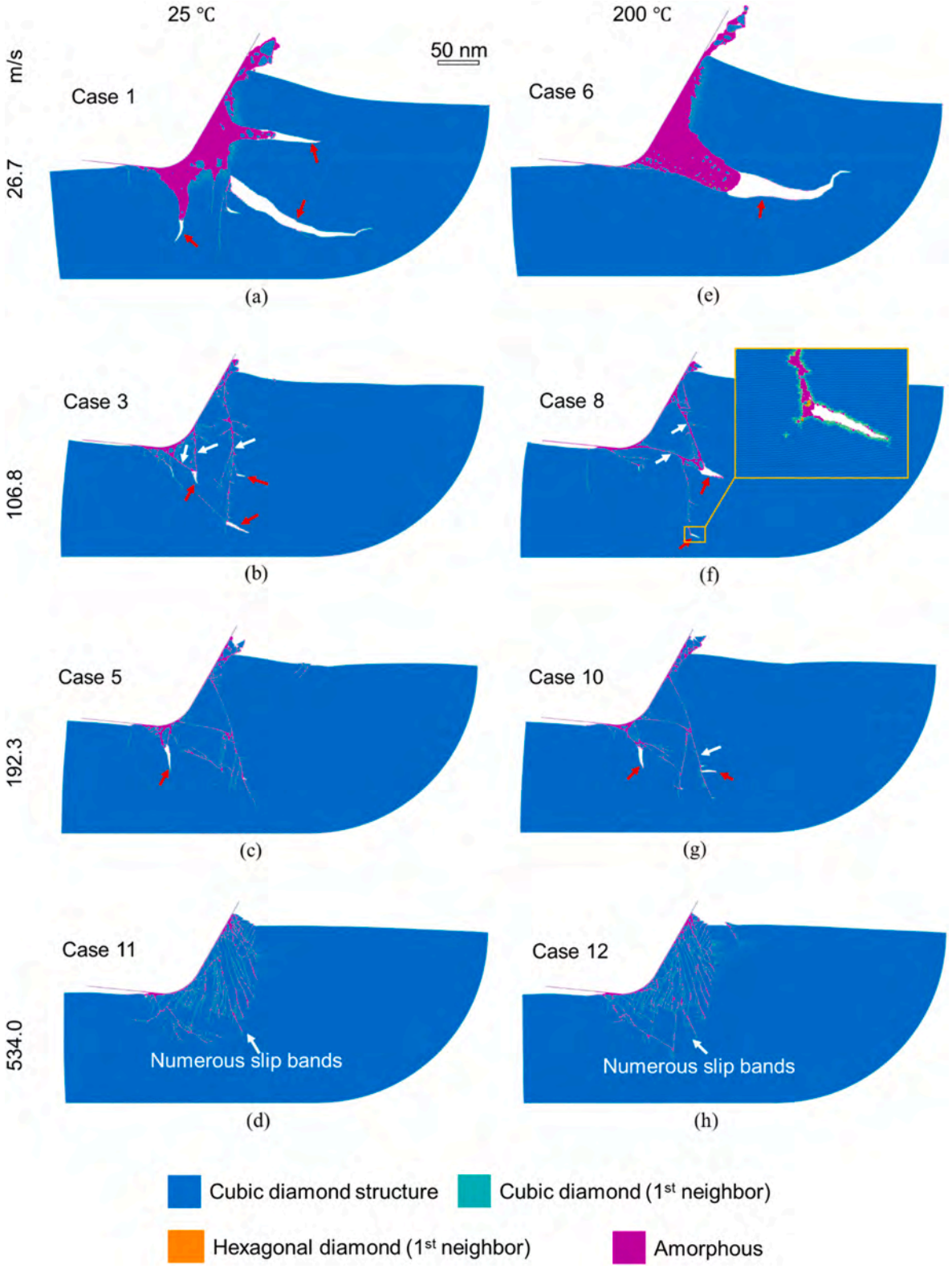

Fig. 9. MD simulation results at different grinding speeds and IMTs. (a)–(d) show the cracks in the RTG cases; (e)–(h) show the cracks in the HTG cases. The cases are arranged in ascending order of the grinding speed. Crack suppression was observed with an increase in the grinding speed. For comparison, the distance slid by the abrasive particle in each case was ~68 Å. The red arrows indicate cracking, while the white arrows mark the slip bands. A few hexagonal diamond atoms were found, which cannot be treated as solid evidence to demonstrate phase transformation during grinding. (For interpretation of the references to colour in this figure legend, the reader is referred to the Web version of this article.)

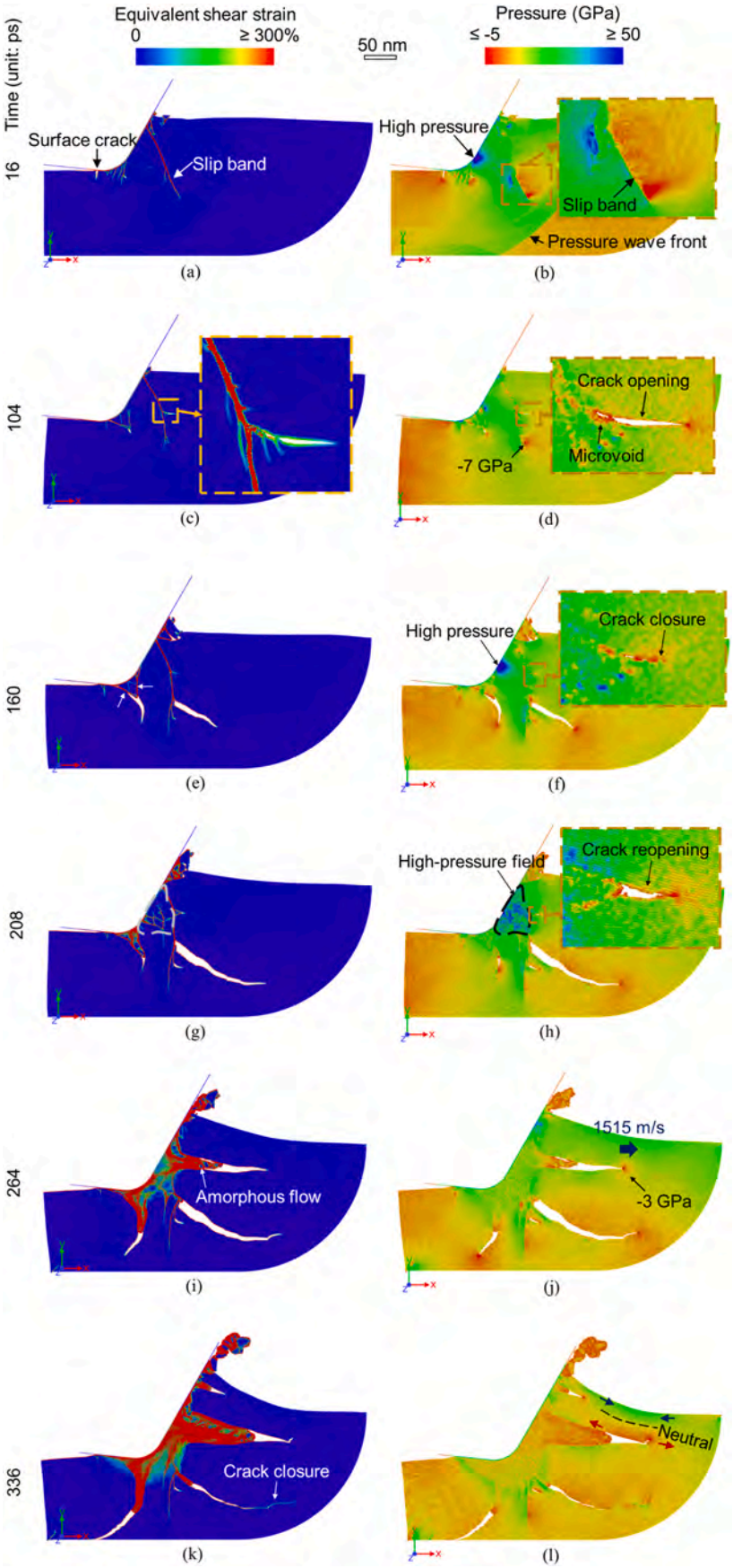

(caption on next page)

Fig. 10. Snapshots of the equivalent strain fields and the pressure fields during grinding for Case 1. The equivalent strain fields are presented in the left column ((a), (c), (e), (g), (i), and (k)) and the pressure field was illustrated in the right column ((b), (d), (f), (h), (j), and (l)) in chronological order. The dashed line in (b) marks the location of the slip band. It shall be noted that the amorphous phase was observed at 264 ps in (i), which was not observed in cases with higher grinding speeds. The reason for this is that the simulation duration for these cases is relatively shorter than that for Case 1, and it may not reach the critical duration of phase transformation. At 336 ps, the abrasive particle had slid by ~90 Å. The equivalent shear strain fields and hydrostatic stress fields (corresponding to negative pressure) for Case 1 can be referred to supplementary videos, Video-1 and Video-2. As a complement, the equivalent shear strain fields and hydrostatic stress fields for Case 6 can be referred to supplementary videos, Video-3 and Video-4.

1 as Fig. 10(h). Because the stretching direction was nearly along the slip band, the direction of crack propagation formed a large angle with respect to the slip bands (Fig. 10 (c)). The above observations based on the MD simulations were supported by those obtained from experiments. The angle was 70.5° for Case 1 (Fig. 4(b)) and ~90° for Case 10 (Fig. 5(b)).

With the grinding speed increased to 192 m/s for Case 10, the high-pressure field was enlarged, covering the upper part of the slip bands (Fig. 11(d)) and resulting in crack suppression in front of the abrasive particle. It is worth noting that, when grinding speed was relatively low (Fig. 9(a) and (b)), the crack that nucleated in front of the abrasive particle had a high probability of causing long cracks. The reason of long-crack formation was that the cracks were on the grinding path of the abrasive particle and were continuously driven by the grinding force until the large chips separated from the workpiece. For Case 10, long cracks nucleated at the upper part of the slip bands were suppressed owing to the presence of high-pressure field. Cracks still formed at the lower part of the slip bands, where the high-pressure field was absent (Fig. 11(c) and (d)). These cracks cannot propagate over a long distance because the stresses were relatively low as the cracks were away from the abrasive particle. In experiments, with increased grinding speed, the topographies in RTG and HTG (Fig. 2) also demonstrated that the large chipping caused by long crack were suppressed prior to chipping caused by short crack.

With increased grinding speed up to 534 m/s (Fig. 12), the high-pressure field could cover most of the slip bands, and the crack nucleation was largely suppressed, as confirmed by Case 12. Therefore, it can be seen that high-pressure field is the key of crack suppression during the high-speed grinding of MS. The mechanism of high-pressure field suppressing crack formation is schematically illustrated in Fig. 13. The intersection of two slip bands and slip-band tip are the potential locations for crack formation (Fig. 13(a)). The potential cracking locations were stretched by the tensile stress, forming cracks dominated by Mode-I. The tensile stress was localized and thus only affected a small region. During high-speed grinding, the high-pressure field covers most of the slip bands (Fig. 13(b)). The introduced high pressure superposes the tensile stress resulting in the local compressive stress, as Fig. 13(b). Therefore, the crack formation was suppressed.

Two issues for Case 12 (Fig. 12) need to be explained. First, slip bands still occurred for Case 12 (Fig. 11). In the experiments, during high-speed grinding (such as the subsurface of Case 10 shown in Fig. 5 (b)), slip bands are not obvious compared with that for Case 1, which implies that the slip bands may not be the major microstructural evolution during high-speed grinding. The discrepancy between experiments and simulations may be attributed to the fact that the simulation model is 2.5D. In the 2.5D model, the dimensions along the z-axis are short and cannot accommodate complex dislocation evolution. Therefore, the microstructural evolution in the simulations is simplified. Second, numerous slip bands occur simultaneously at the early stage of grinding, and these slip bands are confined within the high-pressure field without propagating to deeper locations. Numerous slip bands quickly dissipate the energy induced by high-speed grinding. Severe plastic deformation occurs in each slip band, and the formation of a slip band converts mechanical work to heat. The quick energy dissipation also prevents slip bands from propagating to deeper locations because the input energy is shared by numerous slip bands. The input energy assigned to each slip band is insufficient to drive the slip bands to deeper locations. Relevant studies performed theoretical analysis [38,39] and conducted shock experiments [40,41]. In these studies, the adiabatic shear band played a role similar to that of the slip band for Case 12. These studies validated that the intensity of adiabatic shear bands was positively correlated with the shock speed.

4.2. Brittle–ductile transition of surface and chip materials

In HTG, a large number of flow streaks were observed on the ground surface when the grinding speed reaches 192.3 m/s, as Fig. 14(d). Nevertheless, when the grinding speed was low, flow streaks were not found in Fig. 14(b), implying that the number of flow streaks increased with an increase in the grinding speed. In contrast, flow streaks were absent in the RTG, as Fig. 14(a) and (c). These flow streaks are the chip materials that transforms into the liquid phase. Owing to the liquid state, liquid chips flow onto the surface rather than being removed. During grinding, liquid chips flow to the sides of the grooves, as Fig. 14(d), and a large number of liquid chips flow back into the grooves. Such a flow causes that the boundary between the groove and shoulder to not be evident in Case 10.

For the two cases with identical grinding speeds and two IMTs, the chipping degree in the HTG was lower than that in the RTG. This trend is evident when comparing Cases 4 and 9. This is because the transient grinding temperature (TGT) in the HTG is higher, causing a more severe brittle–ductile transition of the MS for Case 9. The high TGT is also called “peak flash temperature” [24].

The elevation in the TGT on the surface during high-speed grinding is attributed to the adiabatic effect, which depicts the heat caused by mechanical work without sufficient time to transfer. Temperature elevation is the main factor causing the brittle–ductile transition on the surface. Specifically, the brittle–ductile transition temperature (DBTT) of MS is 540 °C [42,43]. If the MS surface reaches a temperature of 540 °C, the MS surface is treated as ductile surface mode grinding, and a trade-off exists between the IMT and temperature caused by work conversion (WCT). The governing equation is given by

$$T_{DBTT} = T_{TGT} = T_{IMT} + T_{WCT} \tag{2}$$

where T_{DBTT} is the ductile–brittle transition temperature; T_{TGT} is the transient grinding temperature; T_{IMT} is the initial material temperature; and T_{WCT} is the temperature caused by work conversion.

The variation in WCT with the grinding speed has been studied for several decades. The earliest study on temperature variations during grinding was conducted by Salomon [44]. Salomon’s conjecture states that the grinding temperature decreases after reaching its peak value. However, controversies still persist [45] because the temperature drop during high-speed grinding has never been validated. Based on reliable experimental results [46], the relationship between the grinding speed and temperature is close to a first-order relationship [47]. In addition, some reports have indicated that temperature saturation may occur at high grinding speeds for certain materials, including low-carbon XC18 [48] and 42CrMo4 steels [49]. The saturation temperature is ~50 % of the melting point. The flow streaks observed for Case 10 (Fig. 4) verify that the grinding temperature of MS can reach the melting point. Temperature saturation does not appear to occur during the grinding of MS. Therefore, the relationship between the grinding speed and WCT can be simplified as a first-order relationship,

$$v_{cr} = kT_{WCT} + b \tag{3}$$

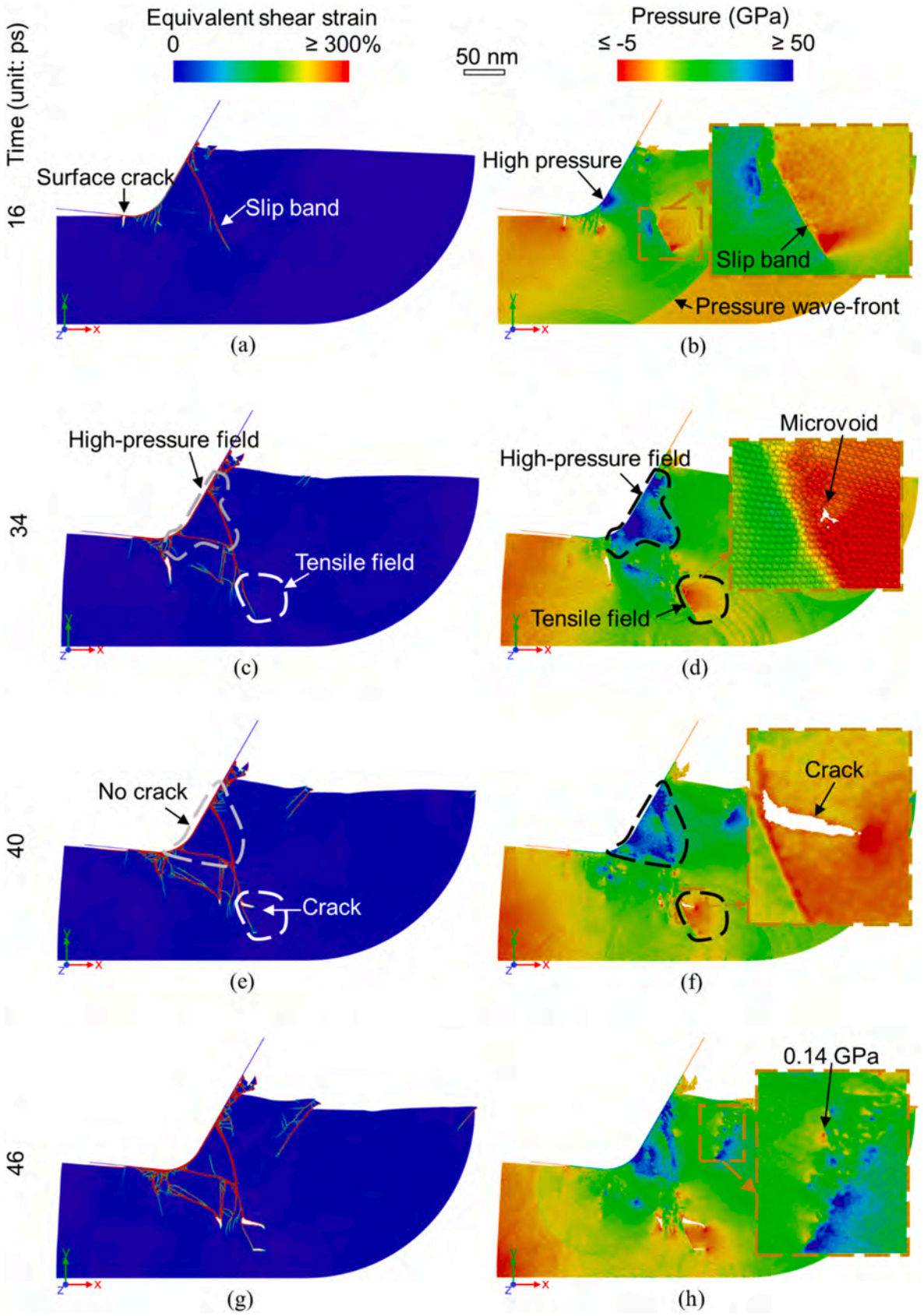

Fig. 11. Snapshots of the equivalent strain fields and pressure fields during grinding for Case 10. The equivalent strain fields are presented in the left column ((a), (c), (e), and (g)), and the pressure fields are illustrated in the right column ((b), (d), (f), and (h)), in chronological order. A high-pressure field occurred in (d). Compared with the high-pressure field for Case 1, the high-pressure field for Case 10 is larger, which is caused by the impact from the abrasive particle during high-speed grinding. The high pressure suppressed crack nucleation within the high-pressure field, as shown in (f). For comparison with Case 1, the abrasive particle had slid by ~88 Å at 46 ps. The equivalent shear strain fields and hydrostatic stress fields for Case 10 can be referred to supplementary videos, Video-5 and Video-6.

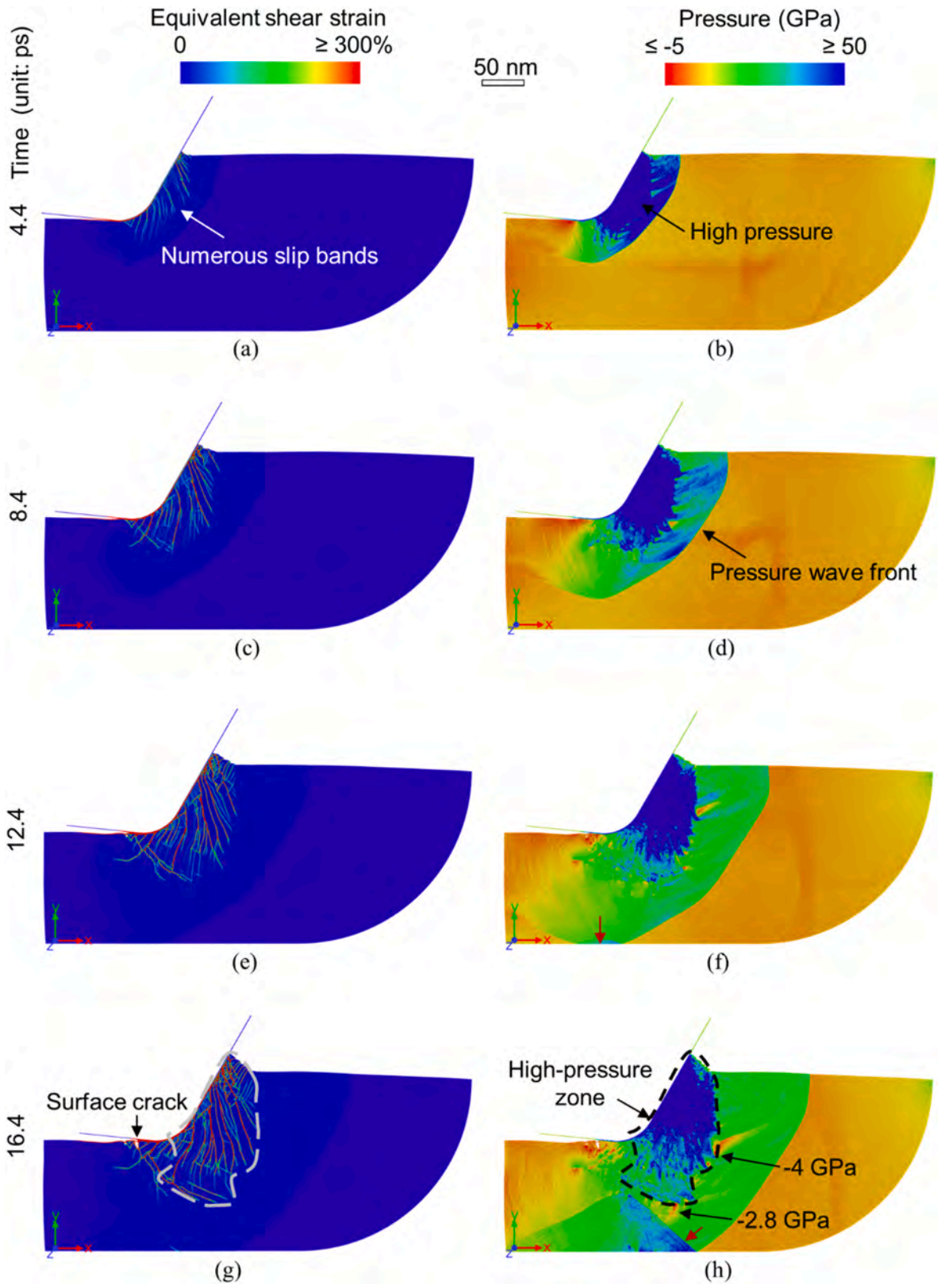

Fig. 12. Snapshots of the equivalent strain fields and pressure fields during grinding for Case 12. The equivalent strain fields are presented in the left column ((a), (c), (e), and (g)), and the pressure fields are illustrated in the right column ((b), (d), (f), and (h)) in chronological order. Numerous slip bands and a large high-pressure field were observed in this case. The high-pressure field covered the most of the slip bands resulting in complete crack suppression. The red arrow in (f) indicates that the pressure wave touches the bottom boundary. The reflected pressure wave in (h) is marked by the red arrow. Because the reflected pressure wave does not reach the region we are interested, the results out of the reflected pressure wave are still valid. For comparison, the abrasive particle had slid by 88 Å at 16.4 ps. The equivalent shear strain fields and hydrostatic stress fields for Case 12 can be referred to supplementary videos, Video-7 and Video-8. (For interpretation of the references to colour in this figure legend, the reader is referred to the Web version of this article.)

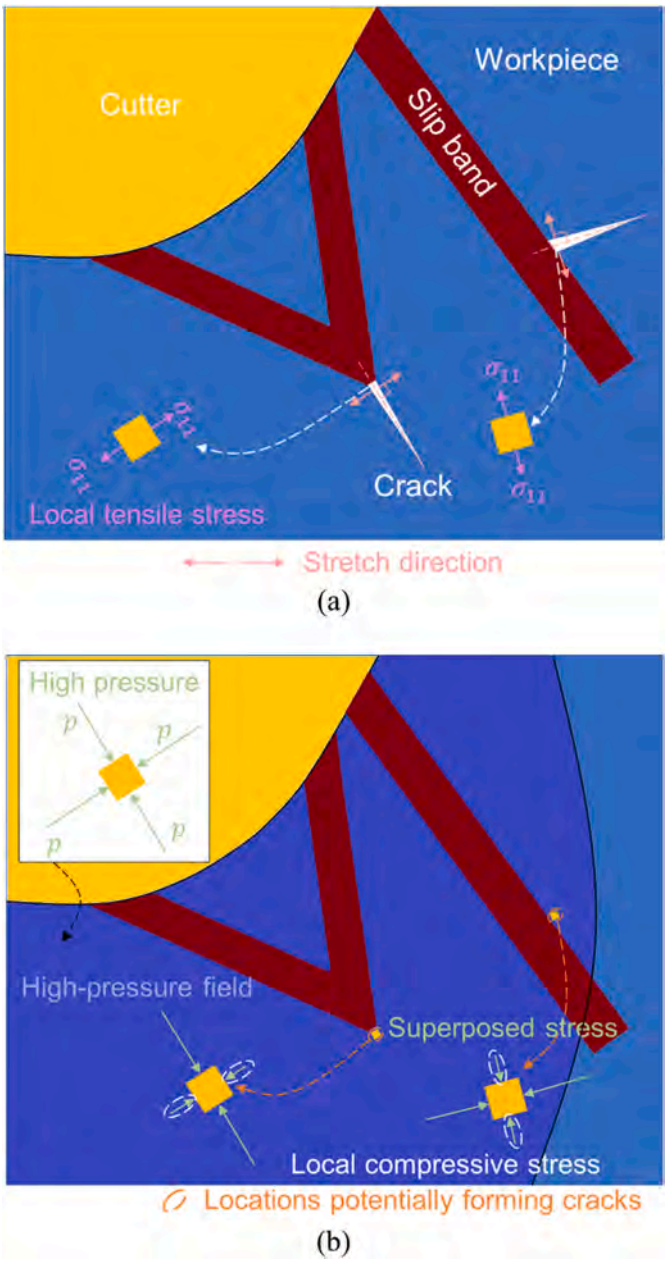

Fig. 13. The schematic illustration showing the mechanism of crack suppression in high-speed grinding. (a) shows the local tensile stress drives the crack formation. (b) shows the crack suppression caused by the change of local tensile stress to the compressive stress, which attributes to the superposition of the high pressure and local tensile stress.

where k is a coefficient, v_{cr} is the critical grinding speed, and b is a parameter. Subsequently, by combining Eqs. (2) and (3), v_{cr} can be expressed in terms of T_{IMT} as

$$v_{cr} = -kT_{IMT} + kT_{DBTT} + b \tag{4}$$

where $T_{DBTT} = 540°C$. Two points can be used to determine this line. One point ($T_{DBTT} = 540°C$, $v_{cr} \approx 0m/s$) is naturally known. If the IMT is at the DBTT, regardless of how slow the grinding speed is, the grinding must be in the ductile mode. Thus, by inserting $T_{DBTT} = T_{IMT} = 540°C$ and $v_{cr} \approx 0m/s$ into Eq. (4), Eq. (4) gives $b = 0$. The other point can be obtained from experiments. In Fig. 2, the crack suppression for Case 9 can be treated as the critical crack suppression. The critical point ($T_{IMT} = 200°C$, $v_{cr} \approx 160.2m/s$) can be used to plot the critical line (Fig. 15). In Fig. 15, the region above the critical line corresponds to the ductile surface mode and the region below the critical line corresponds to the brittle surface mode. Owing to the extremely high grinding speed, which can cause abrasive particle fracture (e.g., Case 5 in Fig. 2), fracture occurs in the top region, which is indicated by the dashed lines in Fig. 15. A higher IMT allows grinding at a higher grinding speed without fracture because higher IMT causes brittle materials to be more compliant. Thus, the dashed line has a positive slope. However, the slope is still empirical and has not yet been experimentally determined.

The ten experimental cases in experiments were classified in to three regimes, as Fig. 15. Cases 1, 2, 3, 4, 6, 7, and 8 falls on the regime of brittle mode; Case 5 falls on the regime of abrasive-particle fracture; Case 9, and 10 falls on the regime of ductile mode. By examining the surface topography changes in Fig. 2, this classification is considered reasonable. Furthermore, with an increase in the IMT, the critical grinding speed decreases, which implies a trade-off between the IMT and critical grinding speed.

In comparison with single-point grinding, multiple abrasive particles of a grinding wheel are successively scratched by a workpiece, which can increase the TGT and further intensify brittle–ductile transition. In addition, multiple abrasive particles may cause the pressure induced by each particle to be superposed, which may increase the pressure on the workpiece and is beneficial for crack suppression. Owing to the higher TGT and pressure in grinding using a grinding wheel, the brittle–ductile transition of chip materials may be achieved at a lower grinding speed.

4.3. Mechanism of crack nucleation at the intersection of two slip bands

It can be observed from Fig. 16(a) that crack nucleation occurred at the intersection of two slip bands. The mechanism of positive normal stress caused by the two intersecting slip bands can be explained by stress superposition. The kinetic analysis shown in Fig. 16(b) indicates that the upper MS block squeezes the lower MS block, causing relative slips within the slip bands. The stress states within the two slip bands were plotted using infinitesimal elements (Fig. 16(b)). The stress states were observed using two local coordinate systems, CS1 and CS2. The shear stress is designated as positive if it is in a counterclockwise rotation. The stress states in CS1 and CS2 can then be defined as

$$\sigma^{I} = \begin{bmatrix} 0 & \tau_1 \\ \tau_1 & 0 \end{bmatrix} \text{and} \sigma^{II} = \begin{bmatrix} 0 & -\tau_2 \\ -\tau_2 & 0 \end{bmatrix} \tag{5}$$

where σ^{I} is the stress tensor within the right slip band observed at CS1 and σ^{II} is the stress tensor within the left slip band observed at CS2. The superposed stress observed by the local coordinate system CS3 in the intersection region (σ^{III}) can be expressed as

$$\sigma^{III} = \mathbf{Q}_1^T \sigma^{I} \mathbf{Q}_1 + \mathbf{Q}_2^T \sigma^{II} \mathbf{Q}_2 \tag{6}$$

Where $\mathbf{Q}_1$ and $\mathbf{Q}_2$ are the coordinate transformation tensors defined as

$$\mathbf{Q}_1 = \begin{bmatrix} \cos(\alpha) & -\sin(\alpha) \\ \sin(\alpha) & \cos(\alpha) \end{bmatrix} \text{and} \mathbf{Q}_2 = \begin{bmatrix} \cos(\beta) & \sin(\beta) \\ -\sin(\beta) & \cos(\beta) \end{bmatrix} \tag{7}$$

Where α and β are the rotation angles from CS1 to CS3 and from CS2 to CS3, respectively, as shown in Fig. 12(a). Based on Eq. (6), the superposed stress at the intersection region is

$$\sigma^{III} = \begin{bmatrix} \tau_1 \sin(2\alpha) + \tau_2 \sin(2\beta) & \tau_1 \cos(2\alpha) - \tau_2 \cos(2\beta) \\ \tau_1 \cos(2\alpha) - \tau_2 \cos(2\beta) & -\tau_1 \sin(2\alpha) - \tau_2 \sin(2\beta) \end{bmatrix} \tag{8}$$

In Eq. (7), the normal stress along the x-axis observed at CS3 corresponds to $\sigma_{11}^{III} = \tau_1 \sin(2\alpha) + \tau_2 \sin(2\beta)$. Since both $\alpha < 90°$ and $\beta < 90°$, σ_{11}^{III} must be positive, this implies that the local material at the intersection region is in a tensile state along the x-direction of CS3, as shown in Fig. 14(c). This tensile stress results in a Mode-I crack. If we assume $\tau_1 = \tau_2 = \tau$ and $\alpha = \beta$, then the stress tensor in the intersection region is reduced to

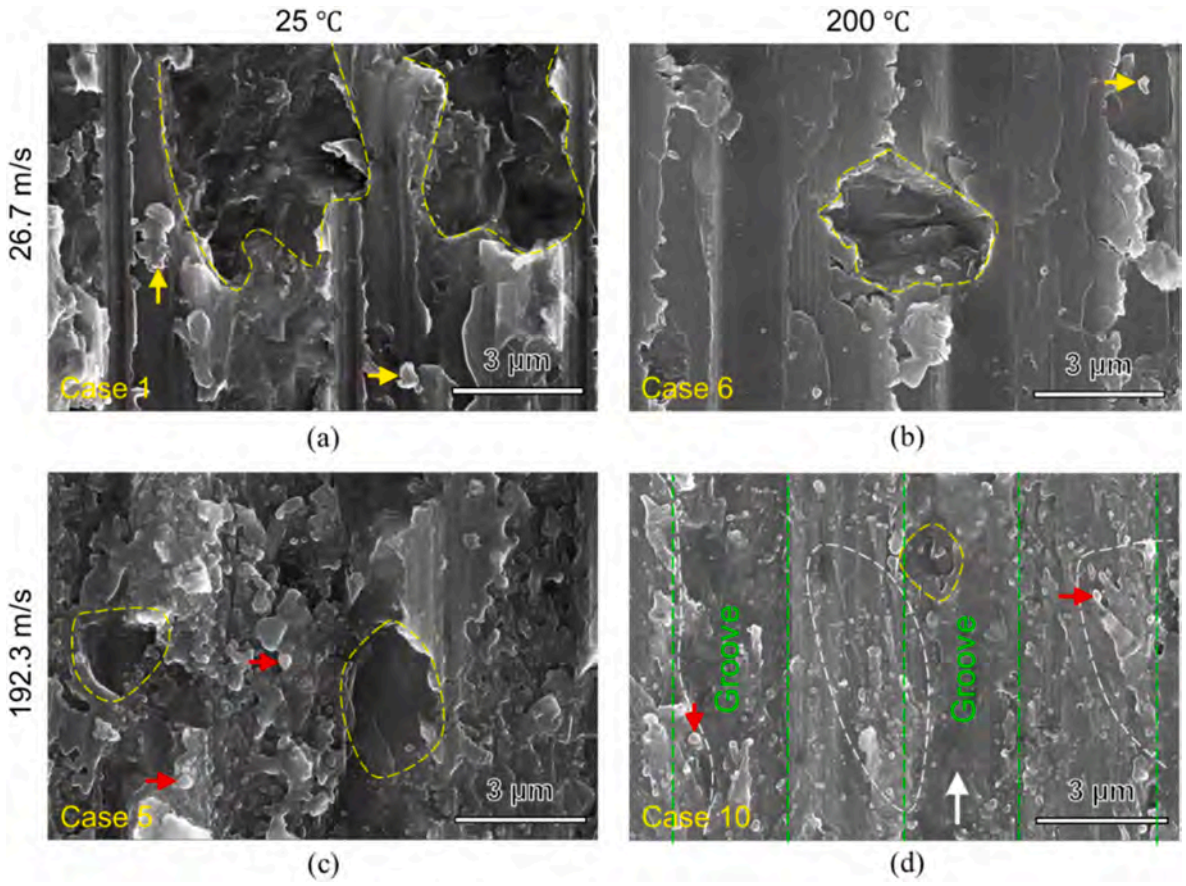

Fig. 14. Local topographies of the ground surfaces. Local topographies for (a) Case 1, (b) Case 6, (c) Case 5, (d) Case 10. The yellow dashed lines in (a), (b), (c), and (d) mark the chippings; the yellow arrows in (a) and (b) indicate the chips; the red arrows in (c) and (d) indicate chip spheroidization; the white dashed lines in (d) mark the flow streaks; the white arrow in (d) indicates the grinding direction. (For interpretation of the references to colour in this figure legend, the reader is referred to the Web version of this article.)

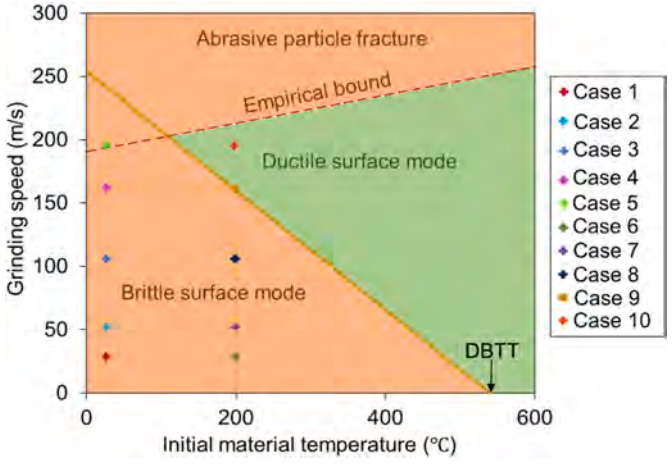

Fig. 15. Trade-off between IMT and critical grinding speed for grinding within the ductile surface mode. The plot is based on a DOC of 1 μm. The points of Case 9 and DBTT were used to separate brittle and ductile surface mode.

$$\sigma^{III} = \begin{bmatrix} 2\tau \sin(2\alpha) & 0 \\ 0 & -2\tau \sin(2\alpha) \end{bmatrix} \tag{9}$$

In this case, no shear stress was observed at CS3 in the intersection region. A crack formed by the intersection of two slip bands did not occur in the experiments in this study, but this phenomenon occurred during grinding of monocrystalline YAG [19].

5. Conclusions

To elucidate the underlying mechanism of crack formation and suppression during grinding of brittle materials, a series of single-point grinding experiments were performed in this study, and both the surface and subsurface of the ground MS were observed using SEM and TEM. To understand the process of crack formation and suppression, large-scale MD simulations were conducted, which demonstrated that pressure (hydrostatic stress) played a vital role in crack formation and suppression. The major conclusions drawn from the experiments and simulations are as follows.

- A crack can form from a single slip band without interacting with other microstructures. The crack nucleates from the microvoids residing within the slip band. The tensile stress concentrating on one side of the tip of the slip band tip stretches the local material approximately along the propagation direction of the slip band, which drives crack nucleation to form a crack opening, which has a large angle with respect to the slip band. The (111) cleavage plane of MS seems to preferentially accommodate cracks.
- The high-pressure field induced by high-speed grinding can result in crack suppression. The tensile stress adjacent to the slip band driving the crack nucleation to form and grow was superposed by the high-pressure field and thus, no crack nucleation occurred in the high-pressure field. As the grinding speed increased, the portion of the slip bands covered by the high-pressure field increased, which caused the partial crack suppression to transit to the complete crack suppression.

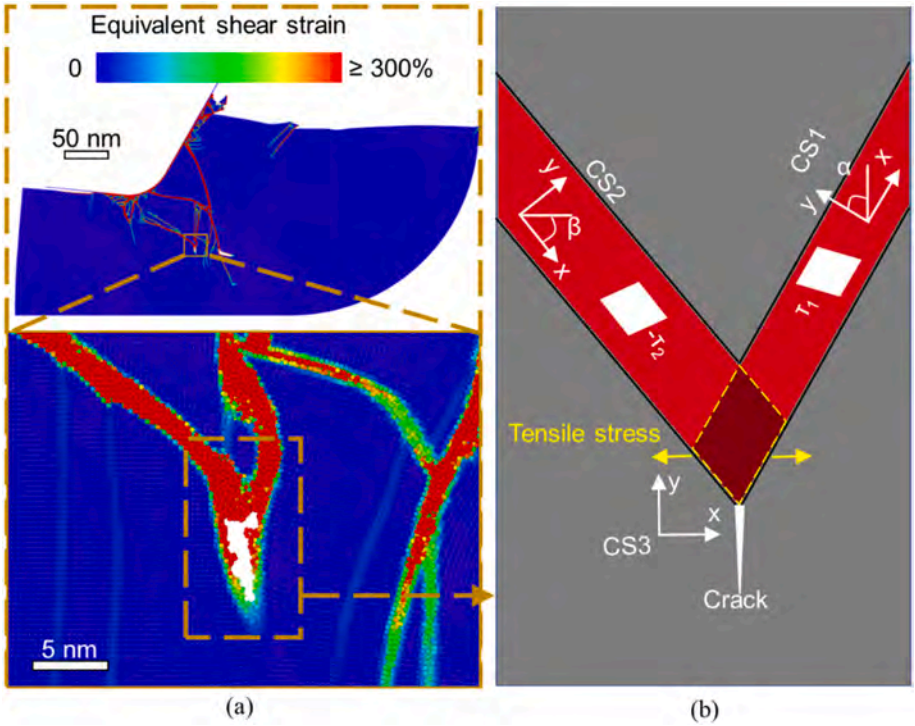

Fig. 16. Crack nucleation mechanism induced by intersection of slip bands. (a) shows two slip bands causing a crack in Case 10; (b) is the kinetic analysis of the slip bands; CS1, CS2, and CS3 in (b) represents the local coordinate systems 1, 2, and 3, respectively.

- Brittle-ductile transition occurred on the surface with an increase in the grinding speed, and a part of the surface material transformed into a liquid state. The surface ductile mode may be achieved through the trade-off between the IMT and grinding speed.
- A crack that formed at the intersection of two slip bands was interpreted by the superposition of the shear stresses in two slip bands.
- This study revealed the fundamental process of crack formation and suppression during grinding of brittle materials, which provides insight on building a 'bottom-up' model based on microstructural evolution to determine the critical DOC during grinding. The model should consider the influence of several factors, such as the abrasive particle geometry, grinding speed, and IMT.

CRediT authorship contribution statement

Jianqiu Zhang: Writing – review & editing, Writing – original draft, Visualization, Validation, Methodology, Investigation, Formal analysis, Data curation. **Xuekun Shang:** Visualization, Methodology. **BinBin He:** Writing – original draft, Resources, Formal analysis. **Bi Zhang:** Supervision, Funding acquisition, Formal analysis.

Declaration of competing interest

The authors declare that they have no known competing financial interests or personal relationships that could have appeared to influence the work reported in this paper.

Data availability

Data will be made available on request.

Acknowledgments

The authors would like to acknowledge the support of the Shenzhen Science and Technology Innovation Commission under project numbers KQTD20190929172505711 and JSGG20210420091802007. The authors also acknowledge the computational power support received from the Center for Computational Science and Engineering of the Southern University of Science and Technology. In addition, we need to acknowledge Dr. Saurav Goel for the discussion on potential functions.

Appendix A. Supplementary data

Supplementary data to this article can be found online at https://doi.org/10.1016/j.ijmachtools.2023.104088.

References

[1] T.G. Bifano, T.A. Dow, R.O. Scattergood, Ductile-regime grinding: a new technology for machining brittle materials, J. Eng. Ind. 113 (1991) 184–189, https://doi.org/10.1115/1.2899676.
[2] B.R. Lawn, A.G. Evans, D.B. Marshall, Elastic/plastic indentation damage in ceramics: the median/radial crack system, J. Am. Ceram. Soc. 63 (1980) 574–581.
[3] D. Hull, D.J. Bacon, Introduction to Dislocations, Butterworth-Heinemann, 2001.
[4] H. Huang, B.R. Lawn, R.F. Cook, D.B. Marshall, Critique of materials-based models of ductile machining in brittle solids, J. Am. Ceram. Soc. 103 (2020) 6096–6100, https://doi.org/10.1111/jace.17344.
[5] B.P. O'Connor, E.R. Marsh, J.A. Couey, On the effect of crystallographic orientation on ductile material removal in silicon, Precis. Eng. 29 (2005) 124–132, https://doi.org/10.1016/j.precisioneng.2004.05.004.
[6] W. Huang, J. Yan, Chip-free surface patterning of toxic brittle polycrystalline materials through micro/nanoscale burnishing, Int. J. Mach. Tool Manufact. 162 (2021), 103688, https://doi.org/10.1016/j.ijmachtools.2020.103688.
[7] H. Mohammadi, D. Ravindra, S.K. Kode, J.A. Patten, Experimental work on micro laser-assisted diamond turning of silicon (111), J. Manuf. Process. 19 (2015) 125–128, https://doi.org/10.1016/j.jmapro.2015.06.007.
[8] X. Chen, C. Liu, J. Ke, J. Zhang, X. Shu, J. Xu, Subsurface damage and phase transformation in laser-assisted nanometric cutting of single crystal silicon, Mater. Des. 190 (2020), 108524, https://doi.org/10.1016/j.matdes.2020.108524.
[9] C. Liu, X. Chen, J. Ke, Z. She, J. Zhang, J. Xiao, J. Xu, Numerical investigation on subsurface damage in nanometric cutting of single-crystal silicon at elevated temperatures, J. Manuf. Process. 68 (2021) 1060–1071, https://doi.org/10.1016/j.jmapro.2021.06.040.
[10] S.J. Lainé, K.M. Knowles, P.J. Doorbar, R.D. Cutts, D. Rugg, Microstructural characterisation of metallic shot peened and laser shock peened Ti–6Al–4V, Acta Mater. 123 (2017) 350–361, https://doi.org/10.1016/j.actamat.2016.10.044.
[11] Q. Liu, Z. Liao, D. Axinte, Temperature effect on the material removal mechanism of soft-brittle crystals at nano/micron scale, Int. J. Mach. Tool Manufact. 159 (2020), 103620, https://doi.org/10.1016/j.ijmachtools.2020.103620.

[12] D. Axinte, P. Butler-Smith, C. Akgun, K. Kolluru, On the influence of single grit micro-geometry on grinding behavior of ductile and brittle materials, Int. J. Mach. Tool Manufact. 74 (2013) 12–18, https://doi.org/10.1016/j.ijmachtools.2013.06.002.
[13] J. Yan, T. Asami, H. Harada, T. Kuriyagawa, Crystallographic effect on subsurface damage formation in silicon microcutting, CIRP Ann 61 (2012) 131–134, https://doi.org/10.1016/j.cirp.2012.03.070.
[14] S. Zhang, W. Zong, Micro defects on diamond tool cutting edge affecting the ductile-mode machining of KDP crystal, Micromachines 11 (2020) 1102.
[15] B. Zhang, H. Tokura, M. Yoshikawa, Study on surface cracking of alumina scratched by single-point diamonds, J. Mater. Sci. 23 (1988) 3214–3224.
[16] M.G. Schinker, Subsurface damage mechanisms at high-speed ductile machining of optical glasses, Precis. Eng. 13 (1991) 208–218, https://doi.org/10.1016/0141-6359(91)90100-W.
[17] H. Huang, L. Yin, L. Zhou, High speed grinding of silicon nitride with resin bond diamond wheels, J. Mater. Process. Technol. 141 (2003) 329–336, https://doi.org/10.1016/S0924-0136(03)00284-X.
[18] I. Zarudi, L.C. Zhang, Effect of ultraprecision grinding on the microstructural change in silicon monocrystals, J. Mater. Process. Technol. 84 (1998) 149–158, https://doi.org/10.1016/S0924-0136(98)00090-9.
[19] C. Li, X. Li, Y. Wu, F. Zhang, H. Huang, Deformation mechanism and force modelling of the grinding of YAG single crystals, Int. J. Mach. Tool Manufact. 143 (2019) 23–37, https://doi.org/10.1016/j.ijmachtools.2019.05.003.
[20] A.L. Gurson, Continuum theory of ductile rupture by void nucleation and growth: Part I—yield criteria and flow rules for porous ductile media, J. Eng. Mater. Technol. 99 (1977) 2–15, https://doi.org/10.1115/1.3443401.
[21] V. Tvergaard, A. Needleman, Analysis of the cup-cone fracture in a round tensile bar, Acta Metall. 32 (1984) 157–169, https://doi.org/10.1016/0001-6160(84)90213-X.
[22] J.R. Rice, D.M. Tracey, On the ductile enlargement of voids in triaxial stress fields, J. Mech. Phys. Solid. 17 (1969) 201–217.
[23] Y. Huang, Accurate dilatation rates for spherical voids in triaxial stress fields, J. Appl. Mech. Trans. ASME. 58 (1991) 1084–1086.
[24] S. Malkin, C. Guo, Grinding Technology: Theory and Application of Machining with Abrasives, Industrial Press Inc., 2008.
[25] L.A. Giannuzzi, F.A. Stevie, A review of focused ion beam milling techniques for TEM specimen preparation, Micron 30 (1999) 197–204, https://doi.org/10.1016/S0968-4328(99)00005-0.
[26] I. Zarudi, L.C. Zhang, Structure changes in mono-crystalline silicon subjected to indentation — experimental findings, Tribol. Int. 32 (1999) 701–712, https://doi.org/10.1016/S0301-679X(99)00103-6.
[27] H. Izumi, T. Kita, S. Arai, K. Sasaki, S. Kamiya, The origin of fatigue fracture in single-crystal silicon, J. Mater. Sci. 57 (2022) 8557–8566, https://doi.org/10.1007/s10853-022-07055-5.
[28] R. Chen, J. Wang, F. Fang, X. Zhang, Influence of buried modified layer on crack propagation and diamond turning of silicon, Precis. Eng. 55 (2019) 426–432, https://doi.org/10.1016/j.precisioneng.2018.10.011.
[29] F.H. Stillinger, T.A. Weber, Computer simulation of local order in condensed phases of silicon, Phys. Rev. B 31 (1985) 5262–5271, https://doi.org/10.1103/PhysRevB.31.5262.
[30] B. Lee, R.E. Rudd, First-principles study of the Young's modulus of Si ⟨001⟩ nanowires, Phys. Rev. B 75 (2007), 041305, https://doi.org/10.1103/PhysRevB.75.041305.
[31] J.A. Hauch, D. Holland, M.P. Marder, H.L. Swinney, Dynamic fracture in single crystal silicon, Phys. Rev. Lett. 82 (1999) 3823–3826, https://doi.org/10.1103/PhysRevLett.82.3823.
[32] P. Erhart, K. Albe, Analytical potential for atomistic simulations of silicon, carbon, and silicon carbide, Phys. Rev. B 71 (2005), 035211, https://doi.org/10.1103/PhysRevB.71.035211.
[33] P.M. Agrawal, L.M. Raff, R. Komanduri, Monte Carlo simulations of void-nucleated melting of silicon via modification in the Tersoff potential parameters, Phys. Rev. B 72 (2005), 125206, https://doi.org/10.1103/PhysRevB.72.125206.
[34] J. Wang, X. Zhang, F. Fang, Molecular dynamics study on nanometric cutting of ion implanted silicon, Comput. Mater. Sci. 117 (2016) 240–250, https://doi.org/10.1016/j.commatsci.2016.01.040.
[35] H.J. Berendsen, J. van Postma, W.F. Van Gunsteren, A. DiNola, J.R. Haak, Molecular dynamics with coupling to an external bath, J. Chem. Phys. 81 (1984) 3684–3690.
[36] S. Goel, X. Luo, A. Agrawal, R.L. Reuben, Diamond machining of silicon: a review of advances in molecular dynamics simulation, Int. J. Mach. Tool Manufact. 88 (2015) 131–164, https://doi.org/10.1016/j.ijmachtools.2014.09.013.
[37] F.P. Bowden, J.H. Brunton, J.E. Field, A.D. Heyes, Controlled fracture of brittle solids and interruption of electrical current, Nature 216 (1967) 38–42.
[38] A. Molinari, Collective behavior and spacing of adiabatic shear bands, J. Mech. Phys. Solid. 45 (1997) 1551–1575.
[39] T.W. Wright, H. Ockendon, A scaling law for the effect of inertia on the formation of adiabatic shear bands, Int. J. Plast. 12 (1996) 927–934, https://doi.org/10.1016/S0749-6419(96)00034-4.
[40] V.F. Nesterenko, M.A. Meyers, T.W. Wright, Self-organization in the initiation of adiabatic shear bands, Acta Mater. 46 (1998) 327–340, https://doi.org/10.1016/S1359-6454(97)00151-1.
[41] Z. Lovinger, A. Rikanati, Z. Rosenberg, D. Rittel, Electro-magnetic collapse of thick-walled cylinders to investigate spontaneous shear localization, Int. J. Impact Eng. 38 (2011) 918–929, https://doi.org/10.1016/j.ijimpeng.2011.06.006.
[42] J. Samuels, S.G. Roberts, P.B. Hirsch, The brittle–ductile transition in silicon. I. Experiments, Proceedings of the Royal Society of London. A. Mathematical and Physical Sciences 421 (1989) 1–23, https://doi.org/10.1098/rspa.1989.0001.
[43] P.B. Hirsch, S.G. Roberts, J. Samuels, The brittle-ductile transition in silicon. II. Interpretation, Proceedings of the Royal Society of London. A. Mathematical and Physical Sciences 421 (1989) 25–53, https://doi.org/10.1098/rspa.1989.0002.
[44] C.J. Salomon, Process for Machining Metals of Similar Acting Materials when Being Worked by Cutting Tools, 1931, 523594.
[45] J.M. Longbottom, J.D. Lanham, A review of research related to Salomon's hypothesis on cutting speeds and temperatures, Int. J. Mach. Tool Manufact. 46 (2006) 1740–1747, https://doi.org/10.1016/j.ijmachtools.2005.12.001.
[46] M.A. Davies, T. Ueda, R. M'Saoubi, B. Mullany, A.L. Cooke, On the measurement of temperature in material removal processes, CIRP Ann 56 (2007) 581–604, https://doi.org/10.1016/j.cirp.2007.10.009.
[47] T. Ueda, A. Hosokawa, K. Yamada, Effect of oil mist on tool temperature in cutting, J. Manuf. Sci. Eng. 128 (2005) 130–135, https://doi.org/10.1115/1.2039099.
[48] N. Ranc, V. Pina, G. Sutter, S. Philippon, Temperature measurement by visible pyrometry: orthogonal cutting application, J. Heat Tran. 126 (2005) 931–936, https://doi.org/10.1115/1.1833361.
[49] G. Sutter, L. Faure, A. Molinari, N. Ranc, V. Pina, An experimental technique for the measurement of temperature fields for the orthogonal cutting in high speed machining, Int. J. Mach. Tool Manufact. 43 (2003) 671–678.